Low-Complexity LMMSE Receiver Design for Practical-Pulse-Shaped MIMO-OTFS Systems

Prem Singh⬤, Shashank Tiwari⬤, and Rohit Budhiraja⬤, *Member, IEEE*

Abstract— Orthogonal time frequency space modulation (OTFS) scheme establishes reliable communication in a rapidly time-varying wireless channel with a high Doppler spread. We design a low-complexity linear minimum mean squared error (LMMSE) receiver for *practical-pulse-shaped* multiple-input multiple-output (MIMO)-OTFS systems. The proposed receiver exploits the inherent channel sparsity and the channel-agnostic structure of matrices involved in the LMMSE receiver, and has only a log-linear complexity. It provides exactly the same solution, and hence the same bit error rate (BER), as that of the conventional LMMSE receiver with a cubic order of complexity. We also derive, by using the Taylor series expansion and the results from random matrix theory, a tight closed-form approximation for the post-processing signal-to-noise-plus-interference ratio (SINR) expression of the proposed receiver. This expression is derived by assuming imperfect receive channel state information. We show using extensive numerical investigations that the derived SINR expression, when averaged over multiple channel realizations, accurately characterizes the BER of a MIMO-OTFS system.

Index Terms— Orthogonal time frequency space (OTFS), minimum mean squared error (MMSE) receiver, low-complexity, signal-to-noise-plus-interference ratio (SINR), bit error rate (BER).

I. Introduction

ORTHOGONAL time frequency space (OTFS) is a two-dimensional waveform which multiplexes symbols in the delay-Doppler domain, and is shown to be robust to the high Doppler spread [1], [2], [3], [4], [5], [6], [7], [8]. This is unlike the widely-popular orthogonal frequency division

multiplexing (OFDM) waveform which multiplexes symbols in the time-frequency domain, and is known to be extremely sensitive to the high Doppler spread. Also, the delay-Doppler domain channel is known to be sparse [9], [10], which can be leveraged to reduce the OTFS channel estimation and receiver design complexity.

Low-complexity OTFS receiver design has recently received significant research attention [5], [6], [7], [8], [9], [10], [11], [12], [13], [14], [15], [16], [17], [18], [19], [20], [21], [22]. The existing low-complexity receiver design literature has considered either ideal-pulse-shaped or practical-pulse-shaped OTFS systems. For ideal pulse shaping, Hadani et al. in [11] simulated the block error rate of sphere decoding (SD) for single-input single-output (SISO)-OTFS systems. Surabhi et al. in [9] proposed a low-complexity linear receiver for SISO-OTFS systems. The work in [10] analyzed the diversity achieved by the maximum-likelihood (ML) receiver in SISO/multiple-input multiple-output (MIMO)-OTFS systems. Reference [14] investigated a reduced-complexity approximation of the maximum a posteriori (MAP) detector for SISO-OTFS systems using the variational Bayes (VB) approach. Reference [15] modeled the OTFS channel matrix in the vector form, and proposed a low-complexity Markov chain Monte Carlo sampling (MCMCS) detector for SISO-OTFS systems. Cheng et al. in [16], by using two-dimension fast Fourier transform, designed reduced complexity zero forcing (ZF) and minimum mean squared error (MMSE) equalizers for SISO-OTFS systems. Reference [17] numerically quantified the performance of the message passing (MP) receiver for MIMO-OTFS systems. References [18] and [19] investigated low-complexity linear receivers for a MIMO-OTFS system with 2 transmit/receive antennas, and generic number of transmit/receive antennas, respectively.

References [5], [6], [7], [8], [13], [20], [21], [22], in contrast to the aforementioned works, designed low-complexity receivers for practical-pulse-shaped OTFS systems. Reference [5] developed an OTFS signal detector by combining QR decomposition-aided time-domain equalization and maximum ratio combining (MRC). Yao et al. in [6] designed a fractionally-spaced sampling (FSS) OTFS receiver, wherein the sampling rate is an integer multiple of the symbol rate. Gaudio et al. in [7] developed a soft-output MP detector for OTFS-aided radar systems that exploits the delay-Doppler channel sparsity. Tiwari et al. in [8] designed a linear receiver for OTFS systems by exploiting the time-domain channel sparsity. Qu et al. in [20] also exploited the delay-Doppler domain channel matrix sparsity to design a low-complexity

TABLE I
SUMMARY OF LITERATURE FOCUSING ON DATA DETECTION IN OTFS

Ref.	OTFS Variant	CSI	Pulse Shape	Scheme	Analytical BER	Complexity Analysis
[11], [14]	CP- and RCP-SISO	Perfect	Ideal	SD	×	✓
[10]	RCP-SISO	Perfect	Ideal	MP	×	×
[15]	RCP-SISO	Imperfect	Ideal	MCMCS	×	×
[9]	RCP-SISO	Perfect	Ideal	ZF, MMSE	×	✓
[8]	RCP-SISO	Perfect	Practical	MMSE	×	✓
[12], [13]	RCP-SISO	Perfect	Practical	MP	×	✓
[20]	CP-SISO	Perfect	Practical	MMSE-SIC	×	✓
[18]	RCP-MIMO	Perfect	Ideal	ZF, MMSE	×	✓
[10] [15]	RCP-MIMO	Perfect	Ideal	ML,MP	×	×
[19], [28]	RCP-MIMO	Imperfect	Ideal	ZF, MMSE	✓	✓
[21]	RCP-Massive-MIMO	Perfect	Practical	MMSE-SIC	×	✓
[23], [24]	ZP-SISO/MIMO	Imperfect	Practical	MRC	×	✓
Proposed	**RCP-MIMO and CP-MIMO**	**Imperfect**	**Practical**	**MMSE**	✓	✓

MMSE successive interference cancellation (SIC) receiver for SISO-OTFS systems. Reference [12] investigated an MP-aided receiver for SISO-OTFS systems with perfect channel state information (CSI). The MP algorithm reduces the receiver complexity by exploiting the delay-Doppler domain channel sparsity. Pandey et al. in [21] investigated a low-complexity MMSE-SIC receiver for practical-pulse-shaped massive-MIMO systems. The authors in [22] designed a low-complexity channel estimator and MP receiver for a super-imposed pilot-based frame structure. Zhang et al. in [13] proposed a low-complexity SISO-OTFS receiver by combining a matched-filtering-based MP detector with a probability clipping solution. The authors in [23] presented a low-complexity MIMO-OTFS receiver by linearly combining the copies of transmit symbol vectors received through the different diversity branches (propagation paths and receive antennas) using MRC. The MRC receiver combining weights are optimized to combat the adverse effects of the spatial correlation at the receiver. Their designs iteratively improves the signal-to-interference-plus-noise ratio (SINR). The authors in [24] reformulated the OTFS input-output relation, and proposed two versions of a linear-complexity iterative rake detector algorithm for zero-padding (ZP)-OTFS modulation based on MRC. Ramachandran and Chockalingam in [25] designed an iterative MP based receiver for MIMO-OTFS systems by assuming perfect receive CSI. The MP receiver, as shown later, has a much higher computational complexity than the proposed linear MMSE (LMMSE) receiver. Li et al. in [26] proposed a hybrid MAP and parallel interference cancellation (PIC) receiver for SISO-OTFS systems. Their designs exploit the fact that the gains associated with different paths can be highly diverse. These designs, therefore, perform MAP detection only for the paths with large gains, and PIC detection for the remaining paths. Li et al. in [27] investigated a cross time-domain and delay-Doppler (DD) domain iterative receiver for SISO-OTFS systems. Their design estimates channel and detects data in the time domain and DD domain respectively, and iteratively updates the extrinsic information from two domains by using unitary transformations.

In an OTFS system, a cyclic prefix (CP) is added to either each OTFS symbol [20], or to a block of them [10]. The former CP-OTFS systems, experience lesser interference than the latter ones, which are referred to as reduced CP-OTFS (RCP-OTFS) systems. A CP-OTFS system, consequently, has a slightly lower BER. However, for a large number of OTFS symbols per frame or for a large CP overhead, a CP-OTFS system has lower bandwidth efficiency than its RCP counterpart. References [8], [9], [10], [11], [12], [13], [14], [15], [18], [19], [21], [25] designed low-complexity receivers for RCP-OTFS systems, whereas [11] and [20] designed them for CP-OTFS systems.

Table I summarizes the existing OTFS receiver design literature. We see that the [9], [10], [11], [14], [15], [17], [18], [19] designed receivers for SISO/MIMO OTFS systems by assuming ideal transmit/receive pulses. With ideal pulse-shaping, the OTFS channel matrix has a doubly-circulant structure, and can be easily diagonalized using a DFT matrix [18], [19], [28]. This considerably eases the low-complexity linear receiver design for such systems. Ideal pulses, however, cannot be realized in practice due to the time-frequency uncertainty principle [29], [30]. The current work, therefore, considers practical pulse shapes e.g., rectangular [31] or Dirichlet [32] and designs a low-complexity receiver. For practical-pulse-shaped OTFS systems, channel matrix is not doubly-circulant, which significantly complicates their low-complexity linear receiver design. We also see from Table I that only [8], [12], [13], [20] have designed receivers for practical-pulse-shaped OTFS waveform, but that too only for SISO systems. Further, none of the tabulated references have derived analytical BER for OTFS receivers, except [19], [28], which considered only ideal pulse shapes. The closed-form BER expressions are commonly used by system designers to abstract the BER in a time-efficient manner as they can be used to assess realistic performance without actually transmitting data [33]. These expressions are, however, beneficial only if they closely mimic the actual performance. This motivates us to derive analytical BER expressions which can achieve this objective.

To summarize, the existing literature has neither designed low-complexity linear receivers for practical-pulse-shaped CP- and RCP-MIMO-OTFS systems nor analytically derived their BER by considering imperfect receive CSI. Considering the above gaps in the existing MIMO-OTFS literature, this work designs a low-complexity LMMSE receiver for practical-pulse-shaped CP- and RCP-MIMO-OTFS systems, and derives their analytical BER expressions. Further, the proposed LMMSE receiver equalizes data in time-domain, and is applicable for any multi-carrier transmission, provided the matrix $\mathbf{\Psi} = \mathbf{H}^H \mathbf{H} + \rho \mathbf{I}$ has a banded structure, where $\mathbf{H}$ is the channel matrix. The **contributions** of this work are given below:

1) For a practical-pulse-shaped CP- and RCP-MIMO-OTFS system, we design a low-complexity LMMSE receiver by studying the structure of matrices involved in the LMMSE receiver. We show that the most computationally-intensive LMMSE receiver operation is the *inversion of a positive definite multi-banded sparse matrix that has full bandwidth.*[1] We reduce its bandwidth by first proposing a structure matrix of the LMMSE equalization matrix which indicates its sparsity pattern. We then compute a permutation matrix using the structure matrix for re-ordering the multi-banded sparse equalization matrix. We show that structure of the LMMSE equalization matrix is independent of the delay-Doppler locations of propagation paths. This enables us to pre-compute the permutation matrix, which in turn reduces the computational complexity.

2) We show that the proposed LMMSE receiver has $\mathcal{O}(MNN_t \log_2 N)$ computational complexity, which is radically lower than the conventional LMMSE receiver complexity of $\mathcal{O}(M^3 N^3 N_t^3)$. Here M, N and N_t denote the number of delay and Doppler bins, and the transmit antennas, respectively. The proposed LMMSE receiver achieves this complexity without any BER degradation, when compared with its conventional counterpart. This is because it only exploits the inherent properties of the OTFS channel matrix for reducing the complexity, and does not use any approximation. 3) We derive tight closed-form approximate SINR expressions of the LMMSE receivers for CP-MIMO-OTFS and RCP-MIMO-OTFS systems by using i) ideas from random matrix theory; ii) Taylor series expansion; and iii) properties of OTFS channel matrix. We also show that the proposed low-complexity receiver algorithm can also be used to calculate the SINR. We show using extensive simulations that the derived SINR expression, when averaged over multiple channel realizations, accurately calculates the LMMSE receiver BER for both RCP- and CP-MIMO-OTFS systems with imperfect receive CSI.

Notations: The symbols $(\cdot)^T$ and $(\cdot)^\dagger$ denote the transpose and hermitian operations, respectively. The notation $circ\{\mathbf{x}\}$ denotes a circular matrix whose first column is $\mathbf{x}$. The operator $\mathrm{diag}\{\mathbf{x}\}$ creates a diagonal matrix using the elements of $\mathbf{x}$. The operator $vec\{\mathbf{X}\}$ creates a vector by stacking the columns of the matrix $\mathbf{X}$. The symbol $\mathbf{W}_L$ denotes the L-order normalized inverse discrete Fourier transform (IDFT) matrix. The symbols $\mathbb{N}$ and $\mathbb{C}$ denote the natural and complex numbers, respectively; The symbol i) $\mathbf{I}_N$ denotes an $N \times N$ identity matrix; and ii) $\otimes$ denotes the Kronecker product. The notation $\mathbf{X}_{(l,k)}$ extracts the $(l,k)$the entry of the matrix $\mathbf{X}$. The notation $\mathcal{CN}(\mu, \sigma^2)$ denotes a Gaussian random variable with mean μ and variance σ^2.

II. SYSTEM MODEL FOR PRACTICAL-PULSE-SHAPED MIMO-OTFS SYSTEMS

1) MIMO-OTFS Transmission: We consider a MIMO-OTFS system with N_t transmit and N_r receive antennas. Each OTFS frame has a duration of T_f, and contains N symbols of T duration each, such that $T_f = NT$. The OTFS system has a bandwidth of B Hz, which is divided into M sub-carriers of spacing Δf such that $B = M \Delta f$. The uth transmit antenna transmits a QAM symbol $d_u(k,l)$ over the kth Doppler and the lth delay bin. Here $k \in \mathbb{N}[0 \ N-1]$, $l \in \mathbb{N}[0 \ M-1]$ and $u \in [1 \ N_t]$ [17]. The symbols $d_u(k,l)$ have zero mean, and are independent and identically distributed (i.i.d) with power σ_d^2. The symbols $d_u(k,l)$, by using inverse symplectic finite Fourier transform (ISFFT), are mapped to a time-frequency domain symbol $Z_u(n,m)$ as [17]:

$$Z_u(n,m) = \frac{1}{\sqrt{NM}} \sum_{k=0}^{N-1} \sum_{l=0}^{M-1} d_u(k,l) e^{j2\pi[\frac{nk}{N} - \frac{ml}{M}]}. \quad (1)$$

Here $n \in \mathbb{N}[0 \ N-1]$ and $m \in \mathbb{N}[0 \ M-1]$. The time domain signal from the uth antenna is obtained from $Z_u(n,m)$ using the Heisenberg transform as [17]:

$$s_u(t) = \sum_{n=0}^{N-1} \sum_{m=0}^{M-1} Z_u(n,m) g(t-nT) e^{j2\pi m \Delta f(t-nT)}. \quad (2)$$

Here $g(t)$ is the time-domain pulse-shaping filter of duration T. We consider, similar to [12] and [31], a symbol-spaced sampling (SSS) approach with a sampling interval of $T_s = 1/M\Delta f = T/M$ [6]. This leads to transmit and receive pulses of length M samples.

We assume a time-varying channel between the uth transmit and the vth receive antennas which is mathematically modelled as follows [35]:

$$h_{u,v}(\tau, \nu) = \sum_{p=1}^{P} h_p^{(u,v)} \delta(\tau - \tau_p) \delta(\nu - \nu_p). \quad (3)$$

Here, for the pth path between the uth transmit and vth receive antenna: i) h_p is its complex channel gain with $\mathcal{CN}(0,1)$ probability density function (pdf); and ii) τ_p and ν_p are its delay and Doppler values, which are mathematically defined as $\tau_p = \frac{l_p}{M\Delta f}$ and $\nu_p = \frac{k_p}{NT}$ with $l_p \in \mathbb{N}[0 \ M-1]$

---

[1]For an $n \times n$ matrix $\mathbf{A}$ with (i,j)th element given as $a_{i,j}$, if all matrix elements are zero outside a diagonally bordered band whose range is determined by constants k_1 and k_2, i.e., $a_{i,j} = 0$ for $j < i - k_1$ or $j > i + k_2$ with $k_1, k_2 \geq 0$. Then, the parameters k_1 and k_2 are called the lower and upper bandwidth, respectively. The bandwidth of matrix $\mathbf{A}$ is given as $\max(k_1, k_2)$. In other words, it is the number k such that $a_{i,j} = 0$ for $|i-j| > k$ [34].

and $k_p \in \mathbb{R}[0 \; N-1]$. *Note that the parameter k_p models both integer and fraction Doppler values [12].* If $\tau_{\max}$ and $\nu_{\max}$ are the maximum delay and Doppler values, then the maximum channel delay and Doppler lengths for the (u,v)th link are given as $\alpha = \lceil \tau_{\max} M \Delta f \rceil$ and $\beta = \lceil \nu_{\max} N T \rceil$, respectively [8]. The scalar α, which is used to calculate the CP length, plays an important role while designing the proposed low-complexity LMMSE receiver in the sequel. We next discuss the discrete implementation of practical-pulse-shaped MIMO OTFS systems. Before doing that two comments are in order.

Remark 1: References [17], [18], [19], [28] designed low-complexity linear receivers by assuming an ideal $g(t)$ pulse, which satisfies the bi-orthogonality condition [30]. The OTFS channel matrix therein has a doubly-circulant structure which can be diagonalized using the DFT matrices. References [18], [19], [28] exploited this property while designing low-complexity linear receivers. For practical-pulse-shaped OTFS systems, the channel is not doubly circulant, which completely changes their low-complexity linear receiver design. Reference [8] designed a low-complexity LMMSE receiver for practical-pulse-shaped SISO-OTFS systems, wherein the equalization matrix is quasi single-banded. This is unlike the LMMSE equalization matrix for MIMO-OTFS systems which, as shown later in this section, has a multi-banded structure. The design in [8] could also be extended for practical-pulse-shaped MIMO-OTFS systems by using the idea of block-wise inverse from [19] and [28] with a complexity $\mathcal{O}(N_r^2 N_t^2 M^2 N^2)$, which is extremely high for practical values of N_r, N_t, M and N. The current work, however, designs an LMMSE receiver which has a linear complexity in M and N. To achieve this aim, instead of visualizing the MIMO-OTFS channel matrix as blocks of SISO-OTFS channel matrix, we investigate and exploit the inherent properties of the MIMO-OTFS channel matrix. This helps us in inverting the matrices involved in the LMMSE receiver with a low-complexity. The current work, unlike [8], also derives the SINR of the LMMSE receiver in the presence of imperfect receive CSI, and shows that the derived SINR accurately calculates the BER of MIMO-OTFS systems.

Remark 2: We assume, similar to [10], [12], and [31], l_p to be an integer. This is because, similar to them, we consider a wide-band system with $M \Delta f \gg 1$. The sampling time resolution $\frac{1}{M \Delta f}$ is, therefore, sufficient to approximate the path delays to the nearest sampling points [10], [12], [31]. For narrow-band OTFS systems, where delay values cannot be approximated to the nearest integer values, the system model changes significantly [6, Eq. (18)]. Design of low-complexity LMMSE receivers for a practical-pulse-shaped MIMO-OTFS system with off-grid delays requires a separate study, which can be taken up as future work.

2) Discrete Implementation of MIMO-OTFS Systems: We now construct the discrete version of an OTFS system by sampling the time domain transmit signal $s_u(t)$ from (2). We consider a critically-sampled OTFS system with $T \Delta f = 1$, which results in a sampling interval of $\frac{T}{M}$. The samples are collected in a vector $\mathbf{s_u} = [s_u(0) \; s_u(1) \cdots s_u(MN-1)]^{\mathrm{T}}$

as $\mathbf{s}_u = \mathbf{A} \mathbf{d}_u$. Here the vector $\mathbf{d}_u \in \mathbb{C}^{MN \times 1} = vec(\mathbf{D_u} \in \mathbb{C}^{M \times N})$ with the matrix

$$\mathbf{D_u} = \begin{bmatrix} d_u(0,0) & \cdots & d_u(0, N-1) \\ d_u(1,0) & \cdots & d_u(1, N-1) \\ \vdots & \ddots & \vdots \\ d_u(M-1, 0) & \cdots & d_u(M-1, N-1) \end{bmatrix}. \quad (4)$$

The matrix $\mathbf{A} \in \mathbb{C}^{MN \times MN} = \mathbf{W}_N \otimes \mathbf{I}_M$ denotes the OTFS modulation matrix with $\mathbf{W}_N$ being the $N \times N$ IDFT matrix [31]. The transmit vector for N_t antennas is obtained by stacking $\mathbf{s}_u$ as follows: $\mathbf{s} = [\mathbf{s}_1 \; \mathbf{s}_2 \; \cdots \mathbf{s}_{N_t}]^{\mathrm{T}}$. The transmit vector $\mathbf{s}$ can also be written as [31]

$$\mathbf{s} = (\mathbf{I}_{N_t} \otimes \mathbf{A}) \mathbf{d} = \mathbf{B} \mathbf{d}. \quad (5)$$

The vector $\mathbf{d} \in \mathbb{C}^{MNN_t \times 1} = [\mathbf{d}_1^T \; \mathbf{d}_2^T \cdots \mathbf{d}_{N_t}^T]^T$ contains QAM data symbols, and the matrix $\mathbf{B} \in \mathbb{C}^{MNN_t \times MNN_t} = \mathbf{I}_{N_t} \otimes \mathbf{A}$.

Depending upon CP insertion in an OTFS system, it has two popular variants: i) RCP-OTFS which appends a CP of length $L \geq \alpha$ before each OTFS frame, with α being the maximum channel delay spread [12]; and ii) CP-OTFS which appends a CP of length L at the beginning of each OTFS symbol in the frame. We next define a matrix to model the CP addition for both RCP and CP-OTFS systems:

$$\mathbf{C} = \begin{bmatrix} \mathbf{0}_L & \mathbf{I}_L \\ \mathbf{I}_K & \mathbf{0}_K \end{bmatrix}. \quad (6)$$

This matrix appends an L-length CP at the beginning of the K-length vector. The CP addition matrix for RCP-OTFS and CP-OTFS systems are respectively obtained as $\mathbf{C}_{\mathrm{RCP}} = \mathbf{C}$ with $K = MN$, and $\mathbf{C}_{\mathrm{CP}} = \mathrm{blkdiag}[\mathbf{C} \; \mathbf{C} \; \cdots \mathbf{C}]$ with $K = N$. The transmit signals for the RCP-OTFS and CP-OTFS are obtained as $\bar{\mathbf{s}}_{\mathrm{RCP}} = \mathbf{C}_{\mathrm{RCP}} \mathbf{s}$ and $\bar{\mathbf{s}}_{\mathrm{CP}} = \mathbf{C}_{\mathrm{CP}} \mathbf{s}$, respectively. The proposed low-complexity receiver design is applicable for both RCP-OTFS and CP-OTFS systems. We also design a common analysis framework for these two OTFS systems, and to the best of our knowledge, ours is the first work to do so. For brevity, we next design a low-complexity LMMSE receiver for RCP-MIMO-OTFS systems, and subsequently explain how the proposed idea can be extended to design low-complexity receivers for CP-MIMO-OTFS systems.

The received signal vector $\mathbf{r} \in \mathbb{C}^{N_r MN \times 1}$, after removing the CP, is expressed as follows:

$$\mathbf{r} = \mathbf{H} \mathbf{s} + \mathbf{n}, \quad (7)$$

with $\mathbf{H} \in \mathbb{C}^{N_r MN \times N_t MN}$ being the MIMO-OTFS channel matrix and $\mathbf{n} \in \mathbb{C}^{N_r MN \times 1}$ being the additive white Gaussian noise vector with pdf $\mathcal{CN}(\mathbf{0}, \sigma_n^2 \mathbf{I}_{N_r MN})$. The MIMO-OTFS channel matrix $\mathbf{H}$ can now be expressed as follows [17]:

$$\mathbf{H} = \begin{bmatrix} \mathbf{H}_{1,1} & \cdots & \mathbf{H}_{N_t,1} \\ \vdots & \ddots & \vdots \\ \mathbf{H}_{1,N_r} & \cdots & \mathbf{H}_{N_t,N_r} \end{bmatrix}. \quad (8)$$

The channel matrix $\mathbf{H}_{u,v}$ between the uth transmit and the vth receive antennas is [31]:

$$\mathbf{H}_{u,v} = \sum_{p=1}^{P} h_p^{(u,v)} \mathbf{\Pi}^{l_p^{(u,v)}} \mathbf{\Delta}^{k_p^{(u,v)}}. \quad (9)$$

Here $\mathbf{\Pi} = \text{circ}\{[0 \ 1 \ 0 \cdots 0]_{MN \times 1}^T\}$ is the circulant delay matrix, and $\mathbf{\Delta} = \text{diag}\{1 \ e^{j2\pi \frac{1}{MN}} \ \cdots e^{j2\pi \frac{MN-1}{MN}}\}$ is the diagonal Doppler matrix. For an ideal-pulse-shaped OTFS system, the channel matrix $\mathbf{H}_{u,v}$ has a doubly-circulant structure [19], i.e., it consists of M circulant block, each of size $N \times N$. The channel matrix $\mathbf{H}_{u,v}$ for such systems can be easily diagonalized using the FFT matrix [9], which simplifies their low-complexity receiver design [9], [19]. The channel matrix $\mathbf{H}_{u,v}$ for practical-pulse-shaped MIMO-OTFS systems, due to inter-symbol-interference (ISI) and inter-carrier-interference (ICI), is not doubly circulant. Their low-complexity receiver design is radically different from the ideal pulse shaped counterparts.

III. LOW-COMPLEXITY MIMO-OTFS RECEIVER DESIGN FOR RCP-OTFS SYSTEM

The LMMSE estimate of the data vector $\mathbf{d}$ is obtained using (7) as

$$\hat{\mathbf{d}} = \left[(\mathbf{HB})^{\dagger}(\mathbf{HB}) + \frac{\sigma_n^2}{\sigma_d^2}\mathbf{I}_{MNN_t}\right]^{-1}(\mathbf{HB})^{\dagger}\mathbf{r}. \quad (10)$$

We see that the above LMMSE receiver inverts an $MNN_t \times MNN_t$ matrix, which has $\mathcal{O}(M^3N^3N_t^3)$ complexity [36]. For practical systems, subcarriers M, transmit symbols N, and transmit antennas N_t can take large values. This makes the above conventional LMMSE receiver computationally-inefficient. For example, for a typical MIMO-OTFS setting where $M = N = 32$ and $N_t = N_r = 4$, the number of floating point operations (flops) required to calculate the inverse in (10) is $\mathcal{O}(10^{11})$, which is extremely high. The receiver complexity, thus, needs to be significantly reduced for successfully implementing a practical MIMO-OTFS system. We next design a novel low-complexity LMMSE receiver for MIMO-OTFS systems which, *without degrading the BER*, has a reduced computational complexity of $\mathcal{O}(MNN_t \log_2 N_t)$. We achieve this reduction by exploiting the structure of matrices involved in the LMMSE receiver.

We begin this design by demonstrating that the most computationally-complex operation in the LMMSE receiver is the inversion of a full-bandwidth positive definite multi-banded matrix, which, in general, has a cubic order of complexity. We propose a method to reduce the bandwidth of this matrix. The reduced-bandwidth matrix, as shown later, can be inverted with a significantly lower complexity. Note that the proposed idea is different from the exiting studies in [17], [18], [19], and [28] which, by assuming ideal transmit and receive pulse-shapes, exploit the doubly-circulant OTFS channel matrix structure, and diagonalize it using the DFT matrices. As explained above *Remark* 2, the present work is also different from the design in [8], which, if directly extended to design MIMO-OTFS LMMSE receiver, will have $\mathcal{O}(N_r^2N_t^2M^2N^2)$ complexity. This is also extremely high for practical values of N_r, N_t, M and N.

For a practical rectangular or Dirichlet pulse $g(t)$, the matrix $\mathbf{B} = \mathbf{I}_{N_t} \otimes \mathbf{A}$ in (5) becomes unitary. This is because the modulation matrix $\mathbf{A} = \mathbf{W}_N \otimes \mathbf{I}_M$ becomes unitary for such pulses [32]. The LMMSE estimate of the data vector

in (10) thus simplifies to

$$\hat{\mathbf{d}} = \mathbf{B}^{\dagger}\underbrace{[\mathbf{H}^{\dagger}\mathbf{H} + \frac{\sigma_n^2}{\sigma_d^2}\mathbf{I}_{MNN_t}]^{-1}}_{\mathbf{\Psi}}\mathbf{H}^{\dagger}\mathbf{r} = \mathbf{\Phi}\mathbf{r}. \quad (11)$$

Here the matrices $\mathbf{\Psi} \in \mathbb{C}^{MNN_t \times MNN_t} = \mathbf{H}^{\dagger}\mathbf{H} + \frac{\sigma_n^2}{\sigma_d^2}\mathbf{I}_{MNN_t}$ and $\mathbf{\Phi} \in \mathbb{C}^{MNN_t \times MNN_t} = \mathbf{B}^{\dagger}\mathbf{\Psi}^{-1}\mathbf{H}^{\dagger}$. We see from the above expression that the LMMSE receiver can be implemented in two steps:

- First step: LMMSE equalization as follows $\mathbf{y} = \mathbf{\Psi}^{-1}\mathbf{H}^{\dagger}\mathbf{r}$.
- Second step: OTFS matched filtering as follows $\hat{\mathbf{d}} = \mathbf{B}^{\dagger}\mathbf{y}$.

The second step operation $\hat{\mathbf{d}} = \mathbf{B}^{\dagger}\mathbf{y}$ requires only $\frac{MNN_t}{2} \log_2(N)$ complex multiplications [8], and thus has a low implementation complexity. We next propose to implement the first step with low-complexity by splitting it in two steps as i) $\bar{\mathbf{r}} = \mathbf{H}^{\dagger}\mathbf{r}$, and ii) $\mathbf{y} = \mathbf{\Psi}^{-1}\bar{\mathbf{r}}$. We now exploit the inherent structure of the matrices involved therein to design a low-complexity implementation.

Low-complexity implementation of $\bar{\mathbf{r}} = \mathbf{H}^{\dagger}\mathbf{r}$ The vectors $\mathbf{r} \in \mathbb{C}^{MNN_r \times 1}$ and $\bar{\mathbf{r}} \in \mathbb{C}^{MNN_t \times 1}$ can be split as $\mathbf{r} = [\mathbf{r}_1^T \ \mathbf{r}_2^T \ \cdots \mathbf{r}_{N_r}^T]^T$ and $\bar{\mathbf{r}} = [\bar{\mathbf{r}}_1^T \ \bar{\mathbf{r}}_2^T \ \cdots \bar{\mathbf{r}}_{N_t}^T]^T$, respectively. The qth component $\bar{\mathbf{r}}_q \in \mathbb{C}^{MN \times 1}$ of $\bar{\mathbf{r}}$ can be computed using $\mathbf{H}$ expression in (8) as $\bar{\mathbf{r}}_q = \sum_{i=1}^{N_r} \mathbf{H}_{q,i}^{\dagger}\mathbf{r}_i$. It can be expressed using (9) as

$$\bar{\mathbf{r}}_q = \sum_{i=1}^{N_r} \sum_{p=1}^{P} \bar{h}_p^{(q,i)} \mathbf{\Delta}^{-k_p^{(q,i)}} \mathbf{\Pi}^{-l_p^{(q,i)}} \mathbf{r}_i, \ \forall q. \quad (12)$$

Here $\bar{h}_p^{(q,i)}$ denotes the complex conjugate of $h_p^{(q,i)}$. To implement (12), the vector $\mathbf{r}_i$ is first circularly shifted by the matrix $\mathbf{\Pi}^{-l_p^{(q,i)}}$ and then multiplied by the diagonal matrix $\bar{h}_p^{(q,i)} \mathbf{\Delta}^{-k_p^{(q,i)}}$, for each i, p and q using element-wise multiplication. The implementation in (12) requires $\mathcal{O}(PMNN_rN_t)$ complex multiplications.

Low-complexity implementation of $\mathbf{y} = \mathbf{\Psi}^{-1}\bar{\mathbf{r}}$: We first investigate the structure of the matrix $\mathbf{\Psi}$, and then exploit its inherent properties to transform it into a low-bandwidth banded matrix. This will enable us to calculate its low-complexity inverse.

1) Structure of the Matrix $\mathbf{\Psi} = \mathbf{H}^{\dagger}\mathbf{H} + \frac{\sigma_n^2}{\sigma_d^2}\mathbf{I}$: In Fig. 1a, we show the entires of the matrix $\mathbf{H}_{u,v}$ defined in (9). Recall that $\mathbf{H}_{u,v}$ is the constituent matrix of the MIMO-OTFS channel $\mathbf{H}$, and corresponds to the channel between the uth transmit and the vth receive antenna. We see from Fig. 1a that $\mathbf{H}_{u,v}$ is sparse with two bands, with the first and second band being located in the lower and upper triangular regions, respectively. The overall channel matrix $\mathbf{H}$, which is formed by concatenating $\mathbf{H}_{u,v}$ according to (8), will thus contain multiple bands, which are shown in Fig. 1b.

We next discuss the structure of $\mathbf{\Psi}$ in (11), which can be split using (8) as in (13), shown at the bottom of the next page. We see that $\mathbf{\Psi}$ consists of blocks of $MN \times MN$ matrices, and that too of two types: 1) $\mathbf{\Gamma}_u = \sum_{i=1}^{N_r} \mathbf{H}_{u,i}^{\dagger}\mathbf{H}_{u,i} + \frac{\sigma_n^2}{\sigma_d^2}\mathbf{I}_{MN}$,
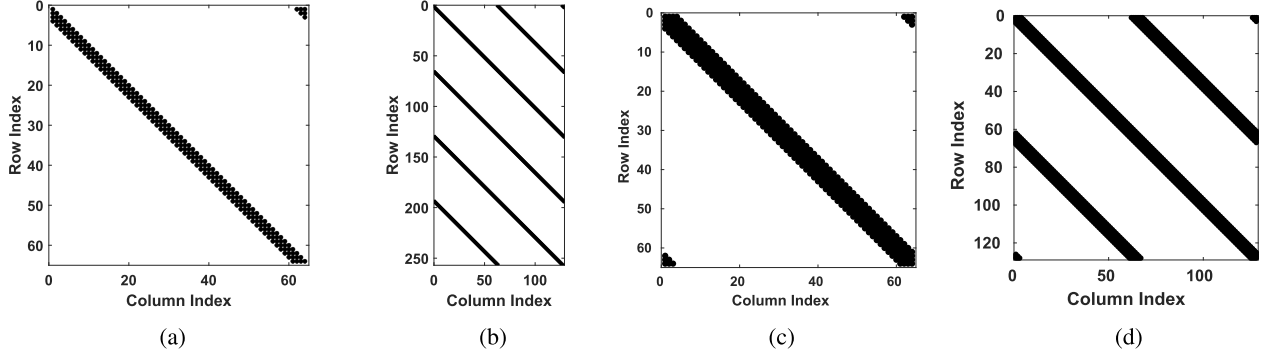
Fig. 1. (a) Channel $\mathbf{H}_{u,v}$ between $u$the transmit and vth receive antenna for $M = 8$, $N = 8$ and $\alpha = 4$. Structure of different matrices involved in LMMSE equalization in RCP-OTFS system for $M = 8$, $N = 8$, $N_t = 2$, $N_r = 4$ and $\alpha = 4$: (b) MIMO channel $\mathbf{H}$; (c) Blocks of $\mathbf{\Psi}$ i.e. $\mathbf{\Gamma}_u$ and $\mathbf{\Upsilon}_{u,u_1}$ in (13); and (d) LMMSE matrix $\mathbf{\Psi}$.
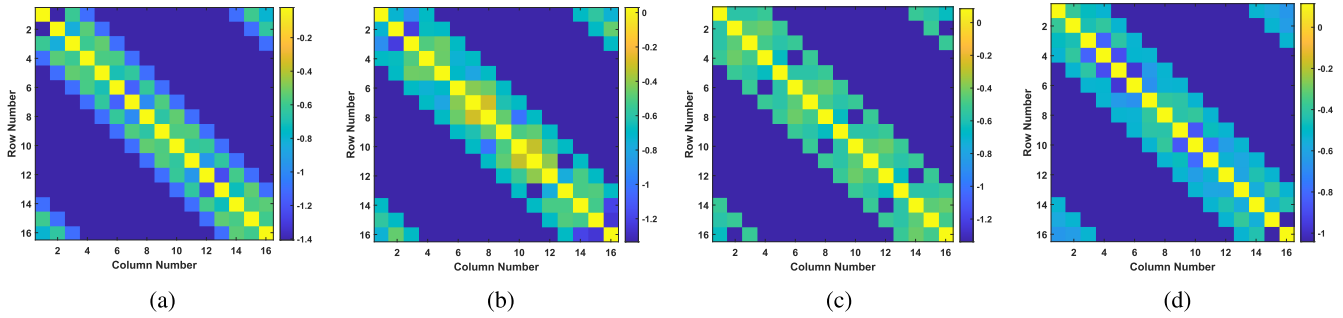
Fig. 2. Structure of the matrix $\mathbf{\Upsilon}_{u,u_1}$ and $\mathbf{\Gamma}_u$ for $M = N = 4, \alpha = 4, P = 3$ and location of propagation path along delay axis is (a) $(2, 3, 4)$, (b) $(1, 2, 3)$, (c) $(1, 3, 4)$, and (d) $(1, 2, 4)$.

and 2) $\mathbf{\Upsilon}_{u,u_1} = \sum_{i=1}^{N_r} \mathbf{H}_{u,i}^{\dagger} \mathbf{H}_{u_1,i}$, where $u, u_1 \in \mathbb{N}[1 \ N_t]$ and $u \neq u_1$. Using (9), $\mathbf{\Upsilon}_{u,u_1}$ is given as

$$\mathbf{\Upsilon}_{u,u_1} = \sum_{i=1}^{N_r} \sum_{p=1}^{P} \sum_{q=1}^{P} \bar{h}_p^{(u,i)} h_q^{(u_1,i)} \mathbf{\Delta}^{-k_p^{(u,i)}}$$
$$\times \mathbf{\Pi}^{-l_p^{(u,i)} + l_q^{(u_1,i)}} \mathbf{\Delta}^{k_q^{(u_1,i)}}. \tag{14}$$

Here $\bar{h}_p^{(u,i)}$ is the complex conjugate of $h_p^{(u,i)}$. Since $\mathbf{\Delta}$ is a diagonal matrix, we observe from (14) that the structure of the matrix $\mathbf{\Upsilon}_{u,u_1}$ depends only on the matrix $\mathbf{\Pi}^{-l_p^{(u,i)} + l_q^{(u_1,i)}}$, which shifts elements of the diagonal matrix $\mathbf{\Delta}$. We also see from (14) that the maximum shift of elements of $\mathbf{\Delta}$ can be $\pm(\alpha - 1)$. Additionally, the matrix $\mathbf{\Pi}$ introduces a cyclic shift. *This leads to the matrix $\mathbf{\Upsilon}_{u,u_1}$, shown in Fig. 1c being quasi-banded with full bandwidth, and with a maximum $2\alpha - 1$ non-zero entries in each row*. Similarly, the matrix $\mathbf{\Gamma}_u$ in $\mathbf{\Psi}$, as also shown in Fig. 1c, is also quasi-banded with full bandwidth. For a typical wireless channel, $\alpha \ll MN$ [30]. Since each block of the matrix $\mathbf{\Psi}$ is sparse, we thus conclude that $\mathbf{\Psi}$

is also a block sparse and a quasi-banded matrix, with its structure shown in Fig. 1d. The maximum number of non-zero entries in each row of $\mathbf{\Psi}$ is $w = N_t(2\alpha - 1)$. Note that irrespective of location of delay values of the propagation paths, the structure of matrix $\mathbf{\Upsilon}_{u,u_1}$ remains same. We explain this using the following example.

Example: Let $M = N = 4$, $\alpha = 4$ and $P = 3$. With this, both $l_p^{(u,i)}$ and $l_q^{(u_1,i)}$ take value in the range $[1, 4]$. However, only three delay values have non-zero channel gain, because $P = 3$. The possible locations of these delay values are $\{(2, 3, 4), (1, 3, 4), (1, 2, 4), (1, 2, 3)\}$. We show in Fig. 2a to Fig. 2d the structure of the matrix $\mathbf{\Upsilon}_{u,u_1}$ or $\mathbf{\Gamma}_u$ when the location of propagation paths along delay axis are $\{(2, 3, 4), (1, 2, 3), (1, 3, 4), (1, 2, 4)\}$ respectively. We see for this figure that irrespective of location of delay values of the propagation paths, the structure of matrix $\mathbf{\Upsilon}_{u,u_1}$ is same, i.e., it is quasi-banded with a maximum $2\alpha - 1 = 7$ non-zero elements in each row or column. Since $\mathbf{\Psi} \in \mathbb{C}^{N_t MN \times N_t MN}$ is constructed using the blocks $\mathbf{\Gamma}_u$ and $\mathbf{\Upsilon}_{u,u_1}$, the above

$$\mathbf{\Psi} = \begin{bmatrix} \sum_{i=1}^{N_r} \mathbf{H}_{1,i}^{\dagger} \mathbf{H}_{1,i} + \frac{\sigma_n^2}{\sigma_d^2}\mathbf{I} & \sum_{i=1}^{N_r} \mathbf{H}_{1,i}^{\dagger} \mathbf{H}_{2,i} & \cdots & \sum_{i=1}^{N_r} \mathbf{H}_{1,i}^{\dagger} \mathbf{H}_{N_t,i} \\ \sum_{i=1}^{N_r} \mathbf{H}_{2,i}^{\dagger} \mathbf{H}_{1,i} & \sum_{i=1}^{N_r} \mathbf{H}_{2,i}^{\dagger} \mathbf{H}_{2,i} + \frac{\sigma_n^2}{\sigma_d^2}\mathbf{I} & \cdots & \sum_{i=1}^{N_r} \mathbf{H}_{2,i}^{\dagger} \mathbf{H}_{N_t,i} \\ & & \ddots & \\ \sum_{i=1}^{N_r} \mathbf{H}_{N_t,i}^{\dagger} \mathbf{H}_{1,i} & \sum_{i=1}^{N_r} \mathbf{H}_{N_t,i}^{\dagger} \mathbf{H}_{2,i} & \cdots \sum_{i=1}^{N_r} \mathbf{H}_{N_t,i}^{\dagger} \mathbf{H}_{N_t,i} + \frac{\sigma_n^2}{\sigma_d^2}\mathbf{I} \end{bmatrix}. \tag{13}$$

analysis implies that the matrix $\mathbf{\Psi}$ is also a quasi-banded matrix, as shown in Fig. 1d.

Although $\mathbf{\Psi}$ is sparse, its inversion still requires $\mathcal{O}(M^3 N^3 N_t^3)$ complex multiplications because its bandwidth is MNN_t, which is equal to the bandwidth of a full matrix of size $MNN_t \times MNN_t$. The proposed design reduces this inversion complexity by exploiting the structure of $\mathbf{\Psi}$.

2) Structure Matrix of $\mathbf{\Psi}$: Recall from the above example that the structure of $\mathbf{\Psi}$ is independent of the instantaneous channel parameters values. This is crucial as it allows us to pre-compute a permutation matrix, which reorders $\mathbf{\Psi}$, and helps in calculating its low-complexity inverse.

We begin by defining the term structure-matrix for a matrix $\mathbf{C} \in \mathbb{C}^{m \times n}$, denoted as $\mathbf{C}_S$, which shows the sparsity pattern of the matrix $\mathbf{C}$. Let the structure-matrix of $\mathbf{\Psi}$ be denoted by $\mathbf{S}$. Our aim is to make $\mathbf{S}$ independent from instantaneous delay values/power delay profile. Note that for a given value of α, multiple power delay profiles are possible. To make $\mathbf{S}$ to be independent of a power delay profile, we consider all possible locations of non-zero entries of $\mathbf{\Psi}$, for a given α. Recall that the structure of matrix $\mathbf{\Psi}$ depends only on $\mathbf{\Pi}^{-l_p^{(u,i)} + l_q^{(u_1,i)}}$, where $-l_p^{(u,i)} + l_q^{(u_1,i)}$ takes value in the range $[-(\alpha-1), (\alpha+1)]$. Thus, to obtain $\mathbf{S}$, we substitute $k_q^{(u_1,i)} = k_p^{(u,i)} = 0$ and $\bar{h}_q^{(u,i)} = \bar{h}_q^{(u_1,i)} = 1$ in the expression of $\mathbf{\Gamma}_u$ and $\mathbf{\Upsilon}_{u,u_1}$. For the (u,u_1)th block $\mathbf{\Upsilon}_{u,u_1}$ in (14) of the matrix $\mathbf{\Psi}$, the structure-matrix is thus given as $\mathbf{S}_{u,u_1} = \sum_{a=-(\alpha-1)}^{\alpha-1} \mathbf{\Pi}^a$, $\forall u, u_1$. Using this property, the structure matrix of $\mathbf{\Psi}$ in (13) can now be obtained as follows

$$\mathbf{S} = \mathbf{1}_{N_t \times N_t} \otimes \sum_{a=-(\alpha-1)}^{\alpha-1} \mathbf{\Pi}^a. \tag{15}$$

Here $\mathbf{1}_{N_t \times N_t}$ is an $N_t \times N_t$ matrix with all-one elements. The structure matrix $\mathbf{S}$ is, therefore, independent of the instantaneous delay values, and is thus known to the receiver beforehand. We use $\mathbf{S}$ to design a low-complexity LMMSE receiver in the next subsection.

3) Low-Complexity Algorithm for $\mathbf{y} = \mathbf{\Psi}^{-1}\bar{\mathbf{r}}$: Recall that the structure of $\mathbf{\Psi}$ depends upon the maximum delay spread α, which is commonly assumed to be known at the receiver [37], [38]. This assumption is practical, as α can easily be estimated using the procedure given in [39] and [40]. The knowledge of α at the receiver implies that the structure of $\mathbf{\Psi}$ is also known at the receiver beforehand. This enables us to design a low-complexity implementation of $\mathbf{y} = \mathbf{\Psi}^{-1}\bar{\mathbf{r}}$.

It is well known that $\mathbf{H}^\dagger \mathbf{H}$, and consequently $\mathbf{\Psi} = \mathbf{H}^\dagger \mathbf{H} + \frac{\sigma_n^2}{\sigma_d^2}\mathbf{I}$, is a positive definite matrix [36]. We propose to reduce the bandwidth of $\mathbf{\Psi}$ by reordering it and then revert the reordering after its inversion. The reordering is performed by using Reverse Cuthil-Mckee algorithm for reordering a Hermitian matrix to a banded matrix [41]. This algorithm computes a permutation matrix $\mathbf{P} \in \mathbb{R}^{MNN_t \times MNN_t}$ to reorder the original matrix $\mathbf{\Psi}$. Interestingly, $\mathbf{P}$ depends only on the structure-matrix $\mathbf{S} \in \mathbb{C}^{MNN_t \times MNN_t}$ of the matrix $\mathbf{\Psi}$ [42], which is known to the receiver beforehand. The permutation matrix $\mathbf{P}$ is computed as $\mathbf{P} = \text{RCuthill\_Mckee}(\mathbf{S})$, where the function RCuthil_Mckee can be implemented offline using an
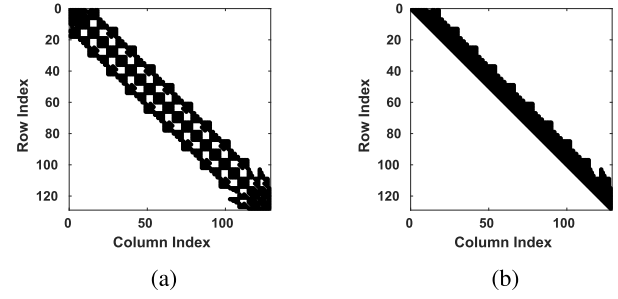

Fig. 3. (a) Reordered LMMSE matrix $\mathbf{G} = \mathbf{P}\mathbf{\Psi}\mathbf{P}^{\mathrm{T}}$ for $\mathbf{\Psi}$ from Fig. 1d; and (b) Upper triangular matrix $\mathbf{U}$ in Cholskey decomposition of $\mathbf{G}$.

in-built MATLAB function *'symrcm'*. We next compute the reordered matrix $\mathbf{G} \in \mathbb{C}^{MNN_t \times MNN_t}$ as

$$\mathbf{G} = \mathbf{P}\mathbf{\Psi}\mathbf{P}^{\mathrm{T}}. \tag{16}$$

In Fig. 3a, we show the structures of the reordered matrices $\mathbf{G}$ for $\mathbf{\Psi}$ from Fig. 1d, which is now converted to a banded matrix $\mathbf{G}$. It follows from [43] that the bandwidth of a matrix after Reverse Cuthill-Mckee transformation is upper bounded by $2w_l$, where w_l is maximum number of entries among rows of the matrix. For the matrix $\mathbf{\Psi}$ with $w_l = N_t(2\alpha - 1)$, the bandwidth of $\mathbf{G}$ is therefor $B_w \leq 2N_t(2\alpha - 1)$. In practice, $B_w \ll MNN_t$, which implies that $\mathbf{G}$ is a sparse matrix. To compute $\mathbf{\Psi}\mathbf{y} = \bar{\mathbf{r}}$, we multiply both sides by $\mathbf{P}$ as $\mathbf{P}\mathbf{\Psi}\mathbf{P}^{\mathrm{T}}\mathbf{P}\mathbf{y} = \mathbf{P}\bar{\mathbf{r}}$. This is because the permutation matrix $\mathbf{P}$ satisfies the following property $\mathbf{P}^T\mathbf{P} = \mathbf{I}_{MNN_t}$ [36]. By substituting $\tilde{\mathbf{r}}_{ce} = \mathbf{P}\mathbf{y}$ and $\bar{\bar{\mathbf{r}}} = \mathbf{P}\bar{\mathbf{r}}$, we get

$$\mathbf{G}\tilde{\mathbf{r}}_{ce} = \bar{\bar{\mathbf{r}}} \implies \tilde{\mathbf{r}}_{ce} = \mathbf{G}^{-1}\bar{\bar{\mathbf{r}}}. \tag{17}$$

Note that $\mathbf{G}$ is a positive definite matrix as permutation retains the positive definiteness of $\mathbf{\Psi}$ [36]. The low-complexity inverse of $\mathbf{G}$ is computed by performing its Cholskey decomposition: $\mathbf{G} = \mathbf{L}\mathbf{U}$, with $\mathbf{U} = \mathbf{L}^{\mathrm{T}}$, which for a banded matrix $\mathbf{G}$ can be computed with $\mathcal{O}(MNN_t B_w^2)$ complex multiplications [36, pp. 180]. It is well known that $\mathbf{L}$ [36, pp. 180] and $\mathbf{U}$ (as shown in Fig. 3b) are also banded matrices with B_w bandwidth. We next exploit the banded structure of $\mathbf{L}$ and $\mathbf{U}$ for low-complexity computation of $\mathbf{G}^{-1}$ as follows:

- calculate $\boldsymbol{\nu} = \mathbf{L}^{-1}\bar{\bar{\mathbf{r}}}$ using the forward substitution algorithm for a banded matrix [44].
- calculate the estimate $\tilde{\mathbf{r}}_{ce} = \mathbf{U}^{-1}\boldsymbol{\nu}$ using the backward substitution algorithm [44].
- calculate the vector $\mathbf{y}$ by reordering $\tilde{\mathbf{r}}_{ce}$ as

$$\mathbf{y} = \mathbf{P}^T\tilde{\mathbf{r}}_{ce}. \tag{18}$$

Both forward and backward algorithms require $\mathcal{O}(MNN_t B_w)$ complex multiplications.

4) Computation of $\hat{\mathbf{d}} = \mathbf{B}^\dagger \mathbf{y}$: The estimate of data vector $\mathbf{d}$ is next computed as $\hat{\mathbf{d}} = \mathbf{B}^\dagger \mathbf{y}$. Using (5), this operation can be equivalently implemented as follows:

$$\hat{\mathbf{d}} = (\mathbf{I}_{Nt} \otimes \mathbf{A}^\dagger)\mathbf{y}. \tag{19}$$

Algorithm 1 Pseudo-Code for Computing, $\hat{\mathbf{d}} = \left[(\mathbf{HB})(\mathbf{HB})^\dagger + \frac{\sigma_n^2}{\sigma_d^2}\mathbf{I}_{MNN_t}\right]^{-1}(\mathbf{HB})^\dagger\mathbf{r}$

Input: Vector $\mathbf{r} \in \mathbb{C}^{MNN_r \times 1}$, Matrix
$\qquad \mathbf{H} \in \mathbb{C}^{MNN_r \times MNN_t}$, Matrix
$\qquad \mathbf{P} \in \mathbb{C}^{\mathbf{MNN_t} \times \mathbf{MNN_t}}$ and $\frac{\sigma_n^2}{\sigma_d^2} \in \mathbb{R}^+$

Output: Vector $\hat{\mathbf{d}} \in \mathbb{C}^{MNN_t \times 1}$

1 Compute: $\boldsymbol{\Psi} = \mathbf{H}^\dagger\mathbf{H} + \frac{\sigma_n^2}{\sigma_d^2}\mathbf{I}$ and $\bar{\mathbf{r}} = \mathbf{H}^\dagger\mathbf{r}$;
2 Reorder: $\mathbf{G} = \mathbf{P}\boldsymbol{\Psi}\mathbf{P}^{\mathrm{T}}$;
3 Compute: $\mathbf{LU} = \mathbf{G}$ using low-complexity Cholskey decomposition [36];
4 Compute: $\tilde{\mathbf{r}}_{ce} = \mathbf{U}^{-1}\mathbf{L}^{-1}\bar{\mathbf{r}}$ using low-complexity forward-backward substitution [44];
5 Reorder: $\mathbf{y} = \mathbf{P}^{\mathrm{T}}\tilde{\mathbf{r}}_{\mathbf{ce}}$;
6 Compute: $\hat{\mathbf{d}} = \mathbf{B}^\dagger\mathbf{y}$ using (19);
7 **return**: $\hat{\mathbf{d}}$

This operation can be implemented using MN_t number of N-point IFFTs [17], and requires $\mathcal{O}(MNN_t \log_2 N)$ complex multiplications. We summarize the proposed receiver in Algorithm 1. Step-1 calculates the matrix $\boldsymbol{\Psi}$, while Step-2 reorders $\boldsymbol{\Psi}$ using $\mathbf{P}$. Step-3 computes the Cholskey decomposition of $\mathbf{G}$, followed by the computation of the vector $\tilde{\mathbf{r}}_{ce}$ and $\mathbf{y}$ in Step-4 and 5, respectively. The estimate of data vector $\mathbf{d}$ is finally obtained in Step-6.

Remark 3: For MIMO-OTFS system with an ideal pulse-shape, the delay-Doppler channel matrix $\mathbf{B}^\dagger\boldsymbol{\Psi}\mathbf{B}$, as shown in [19, Eq. (11)], consists of circular blocks, which can be diagonalised using DFT matrices. The LMMSE matrix for ideal pulse-shaped MIMO-OTFS systems, consequently, inverts a matrix consisting of blocks of $MN \times MN$ diagonal matrices [19, Eq. (13)]. For practical-pulse-shaped MIMO-OTFS systems, the LMMSE receiver, in contrast, inverts a full bandwidth non-circulant matrix $\boldsymbol{\Psi}$. The design of the proposed low-complexity LMMSE receiver is thus radically different than the ones designed in [17], [18], [19], and [28] for ideal pulse shapes. Furthermore, as shown in [9], the BER of OTFS receivers designed by assuming ideal pulse shape is severely degraded, when used for practical-pulse-shaped OTFS systems.

IV. LOW-COMPLEXITY RECEIVER DESIGN FOR CP-OTFS AND CP-OFDM

We now show that Algorithm 1 can also be used for designing low-complexity LMMSE receiver for CP-OTFS based MIMO systems. In fact, Algorithm-1 is independent of the waveform type, as long as the matrix $\boldsymbol{\Psi}$ is multi-banded. This fact is used to also design a low-complexity receiver for CP-OFDM based MIMO systems operating in highly time-varying channels.

Low-complexity LMMSE receiver for MIMO-CP-OTFS systems: A CP-OTFS system, as shown in (6), adds a CP at the beginning of each OTFS symbols. The channel matrix $\mathbf{H}_{u,v} \in \mathbb{C}^{MN \times MN}$ in (9) between the uth transmit and the

vth receive antennas is therefore given as

$$\mathbf{H}_{u,v} = \text{blkdiag}\{\bar{\mathbf{H}}_{u,v}^0,\ \bar{\mathbf{H}}_{u,v}^1,\cdots\ \bar{\mathbf{H}}_{u,v}^{N-1}\}. \quad (20)$$

The matrix $\bar{\mathbf{H}}_{u,v}^q \in \mathbb{C}^{M \times M}$, $q \in \mathbb{Z}[0\ M-1]$ in (9) is expressed as follows [45]:

$$\bar{\mathbf{H}}_{u,v}^q = \sum_{p=1}^P h_p^{(u,v)}\widetilde{\boldsymbol{\Pi}}^{l_p^{(u,v)}} \tilde{\boldsymbol{\Delta}}^{k_p^{(u,v)}} e^{j2\pi\frac{k_p^{(u,v)}(L-l_p)}{(M+L)N}} e^{j2\pi\frac{k_p^{(u,v)}}{N}q}, \quad (21)$$

where $\tilde{\boldsymbol{\Delta}} = \text{diag}\{1\ \ e^{j2\pi\frac{1}{(M+L)N}}\ \ \cdots e^{j2\pi\frac{M-1}{(M+L)N}}\}$ are $\widetilde{\boldsymbol{\Pi}} = \text{circ}\{[0,1,\ldots,0]^T\}$ are Doppler and delay matrices for CP-OTFS transmission [45]. For a CP-OTFS system, the ath component $\bar{\mathbf{r}}_{q,a}$ of the vector $\bar{\mathbf{r}}_q$ in (12) can be computed using (20) as $\bar{\mathbf{r}}_{q,a} = \sum_{i=1}^{N_r} \bar{\mathbf{H}}_{q,i}^{a\dagger}\mathbf{r}_{q,i}$. The vector $\bar{\mathbf{r}}_{q,a}$, after expanding using (21), is implemented by first circularly shifting $\mathbf{r}_{q,a}$ by $\boldsymbol{\Pi}^{-l_p^{(q,i)}}$, and then by multiplying with the diagonal matrix $\bar{h}_p^{(q,i)}\boldsymbol{\Delta}^{-k_p^{(q,i)}}$, for each i, p and q using element-wise multiplication. The implementation of $\bar{\mathbf{r}}_{q,a}$ requires $\mathcal{O}(PMNN_rN_t)$ complex multiplications.

1) Structure of $\boldsymbol{\Psi}$ for CP-OTFS System: We see from Fig. 4a that the MIMO-OTFS channel matrix $\mathbf{H}$ for a CP-OTFS system, similar to an RCP-OTFS system, is also multi-banded. This is because the constituent matrices $\mathbf{H}_{u,v}$ of the MIMO-OTFS channel matrix $\mathbf{H}$ are block-diagonal and sparse. The matrix $\boldsymbol{\Psi}$ in (11) can be rewritten using (20) and (21) as in (22), shown at the bottom of the next page. The matrix $\bar{\boldsymbol{\Gamma}}_{u,q} = \sum_{i=1}^{N_r} \bar{\mathbf{H}}_{u,i}^{q\dagger}\bar{\mathbf{H}}_{u,i}^q + \frac{\sigma_n^2}{\sigma_d^2}\mathbf{I}$; and ii) $\bar{\boldsymbol{\Upsilon}}_{u,u_1,q} = \sum_{i=1}^{N_r} \bar{\mathbf{H}}_{u,i}^{q\dagger}\bar{\mathbf{H}}_{u_1,i}^q$. Also, $u, u_1 \in \mathbb{N}[1\ N_t]$ and $q \in \mathbb{N}[1\ N]$. We see that each $MN \times MN$ block of the matrix $\boldsymbol{\Psi}$ is block diagonal, with each block of size $M \times M$. Using (21), we have

$$\bar{\boldsymbol{\Upsilon}}_{u,u_1,q}$$
$$= \sum_{i=1}^{N_r}\sum_{p=1}^P\sum_{p_1=1}^P \bar{h}_p^{(u,i)}h_{p_1}^{(u_1,i)}\tilde{\boldsymbol{\Delta}}^{-k_p^{(u,i)}}\widetilde{\boldsymbol{\Pi}}^{-l_p^{(u,i)}+l_{p_1}^{(u_1,i)}}$$
$$\times\tilde{\boldsymbol{\Delta}}^{k_{p_1}^{(u_1,i)}}e^{j2\pi\frac{k_{p_1}^{(u_1,i)}l_{p_1}^{(u_1,i)}-k_p^{(u,i)}l_p^{(u,i)}}{(M+L)N}}e^{j2\pi\frac{k_{p_1}^{(u_1,i)}-k_p^{(u,i)}}{N}}. \quad (23)$$

Here $\bar{h}_p^{(u,i)}$ denotes the complex conjugate of $h_p^{(u,i)}$. We see that the structure of $\bar{\boldsymbol{\Upsilon}}_{u,u_1,q}$ depends only on the matrix $\widetilde{\boldsymbol{\Pi}}^{-l_p^{(u,i)}+l_q^{(u_1,i)}}$. This is due to the diagonal nature of $\tilde{\boldsymbol{\Delta}}$. We also see from (23) that the maximum shift of diagonal elements of $\tilde{\boldsymbol{\Delta}}$ can be $\pm(\alpha-1)$. Additionally, since the matrix $\widetilde{\boldsymbol{\Pi}}$ introduces a cyclic shift, *the matrix $\bar{\boldsymbol{\Upsilon}}_{u,u_1,q}$ is quasi-banded with maximum $2\alpha-1$ non-zero entries in each row*. Similarly, the matrix $\bar{\boldsymbol{\Gamma}}_{u,q}$ in $\boldsymbol{\Psi}$, as also shown in Fig. 4b, is also quasi-banded with maximum $2\alpha - 1$ non-zero entries in each row. Also, the matrix $\boldsymbol{\Psi}$, as shown in Fig. 4c, is multi-banded. The total number of non-zero entries in each row of $\boldsymbol{\Psi}$ is $w = N_t(2\alpha - 1)$. Although $\boldsymbol{\Psi}$ is sparse, its matrix inversion still requires $\mathcal{O}(M^3N^3N_t^3)$ complex multiplications due to its $MN(N_t - 1) + M$ bandwidth. The multi-banded structure of $\boldsymbol{\Psi}$ implies that we can use the proposed Algorithm-1 for
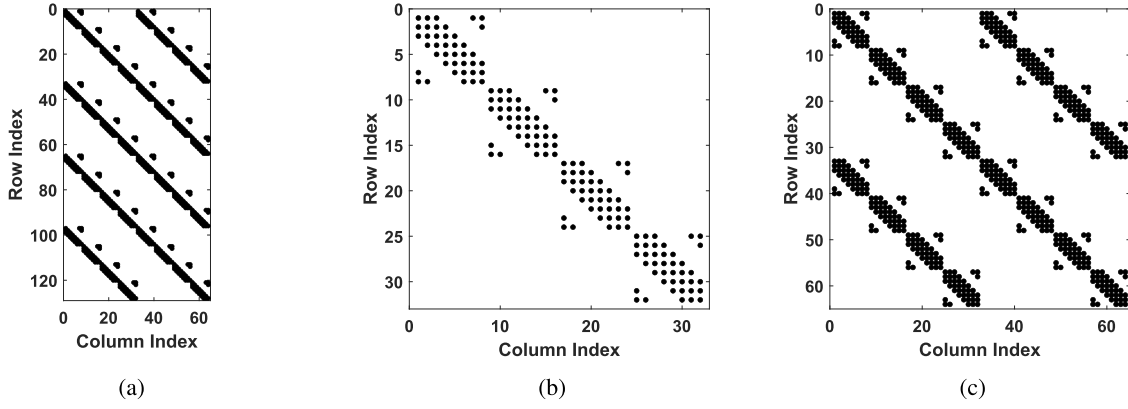
Fig. 4. Structure of matrices involved in the LMMSE receiver in a CP-OTFS system for $M = 8$ subcarriers, $N = 4$ symbols, $N_t = 2$ transmit antennas, $N_r = 4$ receive antennas and $\alpha = 4$: (a) MIMO channel $\mathbf{H}$; (b) Blocks of $\boldsymbol{\Psi}$ i.e. $\bar{\boldsymbol{\Gamma}}_{u,q}$ and $\boldsymbol{\Upsilon}_{u,u1,q}$ in (22); and (c) LMMSE matrix $\boldsymbol{\Psi}$.

TABLE II

COMPUTATIONAL COMPLEXITY OF DIFFERENT RECEIVERS

Scheme	Number of complex multiplications
Conv. LMMSE for MIMO-OTFS	$\frac{MNN_t}{2}\log_2(N) + \frac{2}{3}(MNN_t)^3 + \frac{2}{3}N_t^2 N_r(MN)^3 + 2(MNN_t)^2$
Proposed LMMSE for MIMO-OTFS	$MNN_tN_rP(N_tP+1) + 2MNN_tB_w(B_w+1) + \frac{MNN_t}{2}\log_2 N$
Conv. LMMSE for MIMO-OFDM	$\frac{MNN_t}{2}\log_2(M) + \frac{2}{3}(MNN_t)^3 + \frac{2}{3}N_t^2 N_r(MN)^3 + 2(MNN_t)^2$
Proposed LMMSE for MIMO-OFDM	$MNN_tN_rP(N_tP+1) + 2MNN_tB_w(B_w+1) + \frac{MNN_t}{2}\log_2 M$

designing a low-complexity LMMSE receiver for MIMO-CP-OTFS systems. For this, we next design the structure matrix of $\boldsymbol{\Psi}$.

2) Structure Matrix of $\boldsymbol{\Psi}$ for CP-OTFS Systems: Similar to Sec. III-.2, we can define the structure matrix of $\boldsymbol{\Psi}$ for CP-OTFS systems by taking Doppler values and channel gains in (23) as $k_p^{(u,v)} = 0$ and $h_p^{(u,v)} = 1\ \forall p, u, v$, respectively as

$$\mathbf{S} = \mathbf{1}_{N_t \times N_t} \otimes \left[\mathbf{I}_N \otimes \sum_{a=-(\alpha-1)}^{\alpha-1} \widetilde{\boldsymbol{\Pi}}^a \right]. \tag{24}$$

We use the above structure matrix $\mathbf{S}$ and the matrix $\boldsymbol{\Psi}$ in (22) in Algorithm-1 for the low-complexity implementation of the LMMSE receiver for MIMO-CP-OTFS systems.

LMMSE receiver for MIMO-OFDM over time varying Channel: We know that for a quasi-static channel, a MIMO CP-OFDM system requires one-tap LMMSE receiver. In a rapidly time-varying channel, an OFDM system experiences ICI, which the one-tap equalizer fails to cancel [46]. This necessitates a multi-tap equalizer for MIMO-OFDM receiver in such scenarios, which has an extremely high complexity [47]. We now show that the proposed Algorithm 1 can be used for designing a low-complexity LMMSE receiver for such systems also. The main difference while applying Algorithm 1 lies in the choice of the matched filter matrix $\mathbf{B}$. For OFDM

systems, the unitary matrix $\mathbf{B} = \mathbf{I}_{NN_t} \otimes \mathbf{W}_M$, whereas for the OTFS systems, $\mathbf{B} = \mathbf{I}_{N_t} \otimes \mathbf{W}_M \otimes \mathbf{I}_M$.

For a time-varying MIMO-OFDM system, the estimate $\hat{\mathbf{d}}$ of the data vector in (11) can be obtained by substituting $\mathbf{B}$ as $\mathbf{I}_{N_t} \otimes \mathbf{I}_N \otimes \mathbf{W}_M = \mathbf{I}_{NN_t} \otimes \mathbf{W}_M$ [17]. The proposed low-complexity MIMO-OTFS LMMSE receiver can thus be easily extended to this scenario by simply taking $\mathbf{B} = \mathbf{I}_{NN_t} \otimes \mathbf{W}_M$ in (11). One can thus implement it also for MIMO-OFDM system using these steps. This implies that the estimate $\hat{\mathbf{d}}$ can be calculated as $\hat{\mathbf{d}} = (\mathbf{I}_{NN_t} \otimes \mathbf{W}_M^{\dagger})\mathbf{r}_{ce}$, with NN_t number of M-point FFTs.

V. COMPLEXITY CALCULATION FOR THE PROPOSED LMMSE RECEIVER

We compute the complexity of the proposed LMMSE receiver for MIMO-OTFS and MIMO-OFDM systems in terms of complex multiplications. As shown in Sec. III and Sec. IV, the bandwidth B_w of the matrix $\boldsymbol{\Psi}$ for both CP-OTFS and RCP-OTFS systems is same, and the proposed Algorithm 1 can be used to invert $\boldsymbol{\Psi}$ in both the systems. The computational LMMSE receiver complexity for both CP-OTFS and RCP-OTFS systems is therefore the same. The number of complex multiplications required by the first, third, fourth and sixth steps in Algorithm 1 are $N_tN_rPMN(N_tP+1)$, $2MNN_tB_w^2$, $2MNN_tB_w$, and $\frac{MNN_t}{2}\log_2(N)$, respectively. The reordering

$$\boldsymbol{\Psi} = \begin{bmatrix} \text{blkdiag}\{\bar{\boldsymbol{\Gamma}}_{1,1}, \cdots, \bar{\boldsymbol{\Gamma}}_{1,N}\} & \cdots & \text{blkdiag}\{\bar{\boldsymbol{\Upsilon}}_{1,N_t,1}, \cdots, \bar{\boldsymbol{\Upsilon}}_{1,N_t,N}\} \\ \vdots & \ddots & \vdots \\ \text{blkdiag}\{\bar{\boldsymbol{\Upsilon}}_{N_t,1,1}, \cdots, \bar{\boldsymbol{\Upsilon}}_{N_t,1,N}\} & \cdots & \text{blkdiag}\{\bar{\boldsymbol{\Gamma}}_{N_t,1}, \cdots, \bar{\boldsymbol{\Gamma}}_{N_t,N}\} \end{bmatrix}. \tag{22}$$

operations in (16) and (18) can be implemented without any complex multiplications.

We next compare in Table II the computational complexity of the proposed and conventional (direct implementation) LMMSE receivers for MIMO-OTFS and MIMO-OFDM systems in (11). We see that the proposed MIMO-OTFS receiver requires $\mathcal{O}(MNN_t^2N_rP^2 + MNN_t^3\alpha^2 + MNN_t\log(N))$ complex multiplications, whereas it is $\mathcal{O}(M^3N^3N_t^3)$ for its conventional counterpart. A similar complexity behavior can also be observed for MIMO-OFDM receivers. In a typical situation, wherein $N_t, N_r, P, \alpha \ll MN$, the number of complex multiplications can be approximated as $\mathcal{O}(MNN_t\log(N))$, which is significantly lower than the conventional LMMSE receiver for MIMO-OTFS systems. *This complexity reduction is achieved by exploiting the inherent sparsities in* $\mathbf{H}$ *and* $\mathbf{\Psi}$. We also numerically demonstrate this complexity reduction in the sequel.

VI. BER DERIVATION OF LMMSE RECEIVER WITH IMPERFECT RECEIVE CSI

The SINR expression for the conventional LMMSE receiver for MIMO-OTFS systems inverts the $\mathbf{H}^\dagger\mathbf{H} + \rho\mathbf{I}$ matrix, which has an extremely high computational complexity of $\mathcal{O}(N_t^3M^3N^3)$. We now propose a low-complexity SINR calculation method for the proposed LMMSE receiver, for both RCP-OTFS and CP-OTFS systems,[2] with imperfect CSI using Algorithm 1. We achieve this by first deriving a tight approximation of its SINR expression in a closed-form and by later showing that Algorithm 1 can be used to calculate it. *This complexity reduction is extremely beneficial for a system designer while numerically evaluating the performance of MIMO-OTFS systems for practically implementing them.*

SINR calculation for the proposed LMMSE receiver with imperfect receive CSI: We begin by modelling the MIMO-OTFS channel $\mathbf{H}$ estimate, denoted as $\widehat{\mathbf{H}}$, as follows [48]

$$\widehat{\mathbf{H}} = \mathbf{H} + \Delta\mathbf{H}. \tag{25}$$

The term $\Delta\mathbf{H} \in \mathbb{C}^{N_rMN\times N_tMN}$ is the estimation error matrix, which is independent of $\mathbf{H}$ [48]. The structure of $\Delta\mathbf{H}$ is same as that of $\mathbf{H}$ [19], [28]. We, accordingly, assume that the non-zero entries in a row or column of the block $\Delta\mathbf{H}$ are i.i.d. with pdf $\mathcal{CN}(0, \sigma_e^2)$ [19], [48]. The variance σ_e^2 captures a channel estimator accuracy [48]. We now derive a tight closed-form approximation of the SINR expression. For low-complexity SINR implementation, we use Algorithm 1, which exploits the MIMO-OTFS channel sparsity. We then show that the SINR expression precisely maps the BER of MIMO-OTFS LMMSE receiver, which also validates its tightness.

[2]The SINR derivation of both RCP- and CP-OTSF systems remains same. One has to substitute the corresponding channel matrix $\mathbf{H}_{u,v}$ from (9) and (20) for RCP- and CP-OTFS systems respectively in the SINR expression.

The LMMSE estimate of the transmit vector $\mathbf{d}$ with CSI error can be calculated using (5) and (7) as follows

$$\hat{\mathbf{d}} = \underbrace{\mathbf{B}^\dagger[\widehat{\mathbf{H}}^\dagger\widehat{\mathbf{H}} + \frac{\sigma_n^2}{\sigma_d^2}\mathbf{I}]^{-1}\widehat{\mathbf{H}}^\dagger}_{\widehat{\mathbf{\Phi}}=\mathbf{\Phi}+\Delta\mathbf{\Phi}}(\mathbf{Hs} + \mathbf{n}) = \mathbf{\Phi HBd} + \boldsymbol{\nu}. \tag{26}$$

Here $\mathbf{\Phi} = \mathbf{B}^\dagger\mathbf{\Psi}^{-1}\mathbf{H}^\dagger$ and $\boldsymbol{\nu} = \mathbf{\Phi n} + \Delta\mathbf{\Phi HBd} + \Delta\mathbf{\Phi n}$ is the noise-plus-distortion due to the channel estimation error. The estimated vector $\hat{\mathbf{d}} \in \mathbb{C}^{N_tMN\times 1}$ consists of N_tMN symbols. Let $\hat{d}^{m_{tk}}$ denotes the estimate of the k-th symbol of the t-th stream (antenna), where $m_{tk} = MN(t-1) + k$ with $1 \leq k \leq MN$ and $1 \leq t \leq N_t$. It implies that $1 \leq m_{tk} \leq N_tMN$. The estimate $\hat{d}^{m_{tk}}$ is given in the first expression at the bottom of the next page. We see that the estimated symbol $\hat{d}^{m_{tk}}$ is a function of ISI (i.e., intra-stream interference) from $MN-1$ symbols of the same antenna [12], and ISI from $(N_t - 1)MN$ symbols of other antennas [49]. The ISI is caused due to the non-zero delay and Doppler spreads [12]. By exploiting the relation $\mathbb{E}[\mathbf{dd}^\dagger] = \sigma_d^2\mathbf{I}_{N_tMN}$, the SINR of the kth symbol of tth stream can be expressed as in (27), shown at the bottom of the page, where $\mathbf{R}_\nu = \mathbb{E}[\boldsymbol{\nu\nu}^\dagger]$ represents the covariance matrix of the noise-plus-interference term $\boldsymbol{\nu}$. Since $\mathbf{\Phi} = \mathbf{B}^\dagger\mathbf{\Psi}^{-1}\mathbf{H}^\dagger$, all the terms of the SINR expression in (27), except the noise-plus-interference covariance matrix $\mathbf{R}_\nu$, invert $\mathbf{\Psi}$. We next simplify $\mathbf{R}_\nu$ by using results from random matrix theory [50], and show that its simplified expression also inverts $\mathbf{\Psi}$ matrix. This enables us to apply Algorithm 1 for calculating SINR. For a fixed channel realization, the covariance matrix $\mathbf{R}_\nu = \mathbb{E}[\boldsymbol{\nu\nu}^\dagger]$ can be simplified by using the identity $\mathbf{BB}^\dagger = \mathbf{I}$ as

$$\mathbf{R}_\nu = \sigma_d^2\mathbb{E}[\Delta\mathbf{\Phi HH}^\dagger\Delta\mathbf{\Phi}^\dagger] + \sigma_n^2\mathbf{\Phi\Phi}^\dagger + \sigma_n^2\mathbb{E}[\Delta\mathbf{\Phi}\Delta\mathbf{\Phi}^\dagger]. \tag{28}$$

Since $\mathbf{R}_\nu$ is a function of the matrix $\Delta\mathbf{\Phi}$, we first calculate the $\Delta\mathbf{\Phi}$ expression, and then use it to simplify the first and third terms in (28).

3) Expression for $\Delta\mathbf{\Phi}$*:* The matrix $\widehat{\mathbf{\Phi}}$, as shown in Appendix A, is a function of the matrix $(\mathbf{\Psi} + \mathbf{T})^{-1}$, where $\mathbf{T} = \mathbf{H}^\dagger\Delta\mathbf{H} + \Delta\mathbf{H}^\dagger\mathbf{H}$. As shown in Fig. 5a, the probability that $\frac{||\mathbf{\Psi}^{-1}\mathbf{T}||_F}{MNN_t} \ll 1$ is close to one. This is because both terms in the matrix $\mathbf{T}$ are functions of the error matrix $\Delta\mathbf{H}$. The expression $(\mathbf{\Psi} + \mathbf{T})^{-1}$, as shown in Appendix A, can therefore be approximated using the first-order Taylor series expansion. The empirical CDF of $\frac{||\Delta\mathbf{H}^\dagger\Delta\mathbf{H}||_F}{||\mathbf{H}^\dagger\Delta\mathbf{H}||_F}$ is shown in Fig. 5b. We see that the quantity $\frac{||\Delta\mathbf{H}^\dagger\Delta\mathbf{H}||_F}{||\Delta\mathbf{H}^\dagger\mathbf{H}||_F}$ takes high values with very small probability. Using the above properties, the matrix $\Delta\mathbf{\Phi}$ as shown in Appendix A, is expressed as follows

$$\Delta\mathbf{\Phi} \approx -\mathbf{B}^\dagger\mathbf{\Psi}^{-1}\mathbf{T\Psi}^{-1}\mathbf{H}^\dagger + \mathbf{B}^\dagger\mathbf{\Psi}^{-1}\Delta\mathbf{H}^\dagger. \tag{29}$$

The mathematical justification of the above approximations is beyond the scope of this work, and can be taken up as future work. We next use the above expression for $\Delta\mathbf{\Phi}$ to calculate covariance matrix $\mathbf{R}_\nu$ in (28).
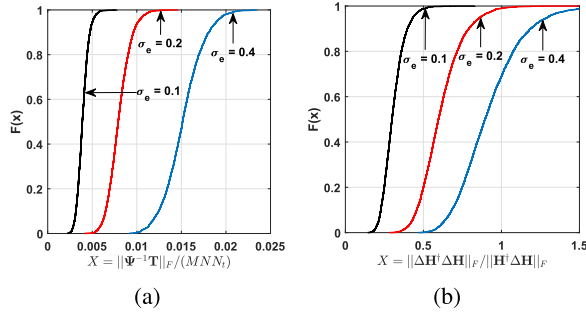
Fig. 5. Empirical CDF plots to validate that (a) $(\mathbf{\Psi} + \mathbf{T})^{-1}$ can be approximated using first-order Taylor series; and b) term $\Delta\mathbf{H}^\dagger\Delta\mathbf{H}$ in (34) can be neglected. For this study, we considered SNR = 0 dB, $M = 32$ subcarriers, $N = 32$ time slots and EVA channel.

4) Calculation of Covariance Matrix $\mathbf{R}_\nu$: We begin by stating the following lemma, which is proved in Appendix-B.

Lemma 1: The first and third terms of the covariance matrix $\mathbf{R}_\nu$ in 28 are given as

$$\mathbb{E}\big[\Delta\mathbf{\Phi}\mathbf{H}\mathbf{H}^\dagger\Delta\mathbf{\Phi}^\dagger]\big] = c_1\,\mathbf{B}^\dagger\mathbf{\Psi}^{-1}\mathbf{\Psi}^{-\dagger}\mathbf{B}$$
$$+ c_2\,\mathbf{B}^\dagger\mathbf{\Psi}^{-1}\mathbf{H}^\dagger\mathbf{H}\mathbf{\Psi}^{-\dagger}\mathbf{B},\text{ and}$$
(30)

$$\mathbb{E}\big[\Delta\mathbf{\Phi}\Delta\mathbf{\Phi}^\dagger\big] = c_3\,\mathbf{B}^\dagger\mathbf{\Psi}^{-1}\mathbf{\Psi}^{-\dagger}\mathbf{B}$$
$$+ c_4\,\mathbf{B}^\dagger\mathbf{H}^\dagger\mathbf{H}\mathbf{\Psi}^{-\dagger}\mathbf{B},$$
(31)

where c_1, c_2, c_3 and c_4 are real-valued constants which are computed as

$$c_1 = c_e\big[\text{trace}\{\mathbf{H}\mathbf{\Psi}^{-1}\mathbf{H}^\dagger\mathbf{H}\mathbf{H}^\dagger\mathbf{H}\mathbf{\Psi}^{-1}\mathbf{H}^\dagger\}$$
$$- 2\,\text{trace}\{\mathbf{H}\mathbf{H}^\dagger\mathbf{H}\mathbf{\Psi}^{-\dagger}\mathbf{H}^\dagger\} + \text{trace}\{\mathbf{H}\mathbf{H}^\dagger\}\big],$$

$$c_2 = c_e\,\text{trace}\{\mathbf{\Psi}^{-1}\mathbf{H}^\dagger\mathbf{H}\mathbf{H}^\dagger\mathbf{H}\mathbf{\Psi}^{-\dagger}\},$$

$$c_3 = c_e\big[\text{trace}\{\mathbf{H}\mathbf{\Psi}^{-1}\mathbf{H}^\dagger\mathbf{H}\mathbf{\Psi}^{-\dagger}\mathbf{H}^\dagger\}$$
$$- 2\,\text{trace}\{\mathbf{H}\mathbf{\Psi}^{-1}\mathbf{H}^\dagger\} + N_r MN\big]$$

$$c_4 = c_e\,\text{trace}\{\mathbf{\Psi}^{-1}\mathbf{H}^\dagger\mathbf{H}\mathbf{\Psi}^{-\dagger}\}.$$
(32)

Here the constant $c_e = \frac{P\sigma_e^2}{MN}$.

Substituting (30) and (31) in (28), we get

$$\mathbf{R}_\nu \approx \sigma_d^2(c_1\,\mathbf{B}^\dagger\mathbf{\Psi}^{-1}\mathbf{\Psi}^{-\dagger}\mathbf{B} + c_2\,\mathbf{B}^\dagger\mathbf{\Psi}^{-1}\mathbf{H}^\dagger\mathbf{H}\mathbf{\Psi}^{-\dagger}\mathbf{B})$$
$$+ \sigma_n^2\mathbf{\Phi}\mathbf{\Phi}^\dagger$$
$$+ \sigma_n^2(c_3\,\mathbf{B}^\dagger\mathbf{\Psi}^{-1}\mathbf{\Psi}^{-\dagger}\mathbf{B} + c_4\,\mathbf{B}^\dagger\mathbf{H}^\dagger\mathbf{H}\mathbf{\Psi}^{-\dagger}\mathbf{B}).$$
(33)

For a fixed channel realization, the SINR of the kth symbol can now be obtained by substituting $\mathbf{R}_\nu$ in (27). The SINR expressions for both RCP- and CP-OTFS systems can be calculated by substituting their respective channel matrix from (9) and (20) in (27). We see that $\mathbf{R}_\nu$ in (33) and the matrix $\mathbf{\Phi}$ in the SINR expression in (27) invert $\mathbf{\Psi}$. We calculate its inverse using the proposed low-complexity Algorithm 1 whose complexity, as shown in Sec. V, is $\mathcal{O}(MNN_t \log_2 N)$. With the SINR expression $\gamma^{m_{tk}}$ in (27), the BER with $2b$-bit QAM constellation in the presence imperfect CSI can now be calculated by plugging $\gamma^{m_{tk}}$ in the following expression $k_0 Q(\sqrt{k_1\gamma^{m_{tk}}})$ [51], where constants $k_0 = \frac{1}{2b}4\left(1 - \frac{1}{2^b}\right)$ and $k_1 = 3/(2^{2b} - 1)$ [52], and $Q(\cdot)$ is the tail of a Gaussian random variable. For example, for 4-QAM with $2b = 2$, the constant $k_0 = 3/2$ and $k_1 = 1$, and for 16-QAM with $2b = 4$, we get $k_0 = 3/4$ and $k_1 = 1/5$. One can similarly calculate k_0 and k_1 for other QAM constellations.

VII. Simulation Results

We now investigate the performance of the proposed low-complexity receivers for both RCP- and CP-OTFS systems. For the studies in the sequel, we consider a spatially multiplexed $N_r \times N_t$ ($N_r \geq N_t$) MIMO-OTFS system with a subcarrier spacing of 15 KHz, which operates at a carrier frequency of 4 GHz. Each OTFS frame has $N \in \{10, 32\}$ time slots, and each time slot has $M \in \{32, 256\}$ subcarriers. The information symbols are drawn from 4-QAM and 16-QAM constellations. The Doppler values are generated using Jake's formula $\nu_p = \nu_{max}\cos(\theta_p)$, where θ_p is uniformly distributed over $[-\pi\ \pi]$ [22]. We consider an Extended Vehicular A (EVA) channel model [53], and a maximum vehicular speed of 500 Kmph. The CP is chosen long enough to accommodate the wireless channel delay spread. The SNR is defined as σ_d^2/σ_n^2.

A. BER Comparison of Proposed and Conventional LMMSE Receivers for Perfect Receive CSI

We perform this study in Fig. 6a and Fig. 6b for 4- and 16-QAM, respectively. Each figure considers two MIMO configurations: i) $N_t = 4$, $N_r = 4$ and ii) $N_t = 2$, $N_r = 4$. We see that the proposed low-complexity LMMSE receiver for MIMO-CP-OTFS, MIMO-RCP-OTFS and MIMO-CP-OFDM systems has exactly the same BER as that of its high-complexity conventional counterpart. This is because the proposed receiver does not make any approximation while equalizing. In particular, as shown in Fig. 6a,

$$\hat{d}^{m_{tk}} = [\mathbf{\Phi}\mathbf{H}\mathbf{B}]_{(m_{tk},m_{tk})}d^{m_{tk}} + \underbrace{\sum_{i=(t-1)MN+1,i\neq k}^{tMN}[\mathbf{\Phi}\mathbf{H}\mathbf{B}]_{(m_{tk},i)}d^i}_{\text{inter-symbol interference}} + \underbrace{\sum_{j=1,j\neq k}^{N_tMN}[\mathbf{\Phi}\mathbf{H}\mathbf{B}]_{(m_{tk},j)}d^j + \nu^{m_{tk}}}_{\text{inter-stream interference}}.$$

$$\gamma^{m_{tk}} = \frac{\sigma_d^2\left|[\mathbf{\Phi}\mathbf{H}\mathbf{B}]_{(m_{tk},m_{tk})}\right|^2}{\sigma_d^2\sum_{i=(t-1)MN+1,i\neq k}^{tMN}\left|[\mathbf{\Phi}\mathbf{H}\mathbf{B}]_{(m_{tk},i)}\right|^2 + \sigma_d^2\sum_{j=1,j\neq i}^{N_tMN}\left|[\mathbf{\Phi}\mathbf{H}\mathbf{B}]_{(m_{tk},j)}\right|^2 + [\mathbf{R}_\nu]_{(m_{tk},m_{tk})}}.$$
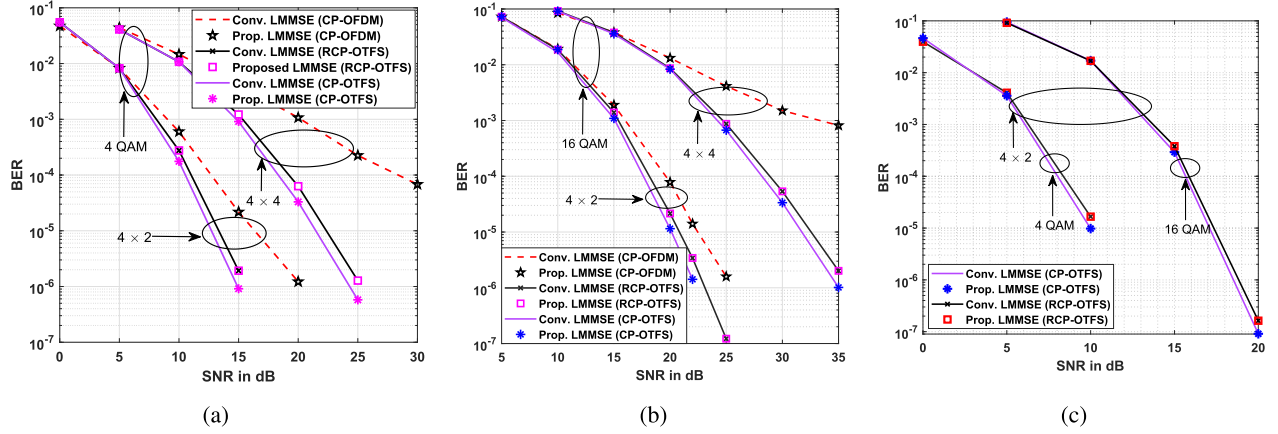(27)

Fig. 6.   BER comparison of the proposed and conventional LMMSE receivers for: (a) 4-QAM; (b) 16-QAM; and (c) 4-QAM and 16-QAM. We assume a vehicular speed of 500 kmph, perfect receive CSI and EVA channel. We consider $M = 32$ subcarriers and $N = 32$ time slots for the first two figures, and $M = 256$ subcarriers and $N = 10$ time slots for the last one.
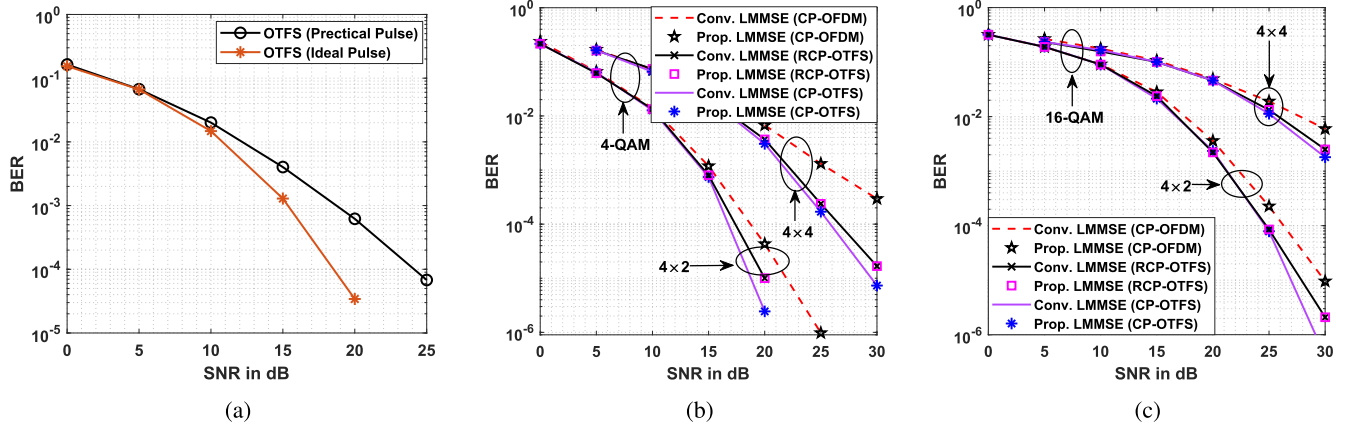

Fig. 7.   (a) BER comparison of the proposed LMMSE receiver for MIMO-OTFS with ideal and practical pulse shaping: 4-QAM, $P = 5$, perfect CSI and uniform power delay profile. BER comparison of the proposed and conventional LMMSE receivers for MIMO-OTFS systems for (b) 4-QAM; (c) 16-QAM. We assume a vehicular speed of 500 kmph, imperfect receive CSI and EVA channel with $M = 32$ subcarriers and $N = 32$ time slots.

the proposed and conventional LMMSE receivers attain a BER of 10^{-4} for 4×2 and 4×4 RCP-OTFS systems at SNR $= 10.8$ dB and SNR $= 19.6$ dB, respectively. We also see that for a rapidly time varying channel, an OTFS system vastly outperforms its OFDM counterpart. For example, a 4×4 MIMO-OTFS system requires 10 dB lower SNR to achieve a BER of 6×10^{-5} and 10^{-3} for 4 and 16-QAM systems respectively, than its MIMO-OFDM counterpart. Further, a 4-QAM 4×2 MIMO-OTFS system requires 5 dB lower SNR to achieve a BER of 10^{-6} than its OFDM counterpart. Note that an OTFS system achieves these gains without any increase in the computational complexity.

We show in Fig. 6c that the BER of the proposed and conventional LMMSE receivers match for an OTFS frame with a higher number of subcarrier and lower number of time slots i.e., $M = 256$ and $N = 10$, respectively. This result shows the efficacy of the proposed receiver for different OTFS subcarrier and time slots configurations. We finally compare in Fig. 7a the LMMSE receiver BER for both ideal- and practical-pulse-shaped MIMO-OTFS systems. We see that the ISI and ICI in

practical-pulse-shaped OTFS system, degrade its BER, when compared with its ideal counterpart.

B. BER Comparison of Proposed and Conventional LMMSE Receivers for Imperfect Receive CSI

In Fig. 7b and Fig. 7c, we extend the study in Fig. 6 for imperfect receive CSI case. The channel estimate, as shown in (25), is modeled as $\widehat{\mathbf{H}} = \mathbf{H} + \mathbf{\Delta H}$. The channel estimation error variance for generating $\mathbf{\Delta H}$ is set as $\sigma_e^2 = 1/(N_t * \text{SNR})$ [19]. We see from Fig. 7b and Fig. 7c that the BER of the proposed and conventional LMMSE receivers matches again for both MIMO-OTFS and MIMO-OFDM systems. An OTFS system still has a significantly lower BER than OFDM. For example in Fig. 7(b) with 4-QAM, the proposed receiver has a BER of 10^{-4} for i) 4×2 and 4×4 RCP-OTFS systems at SNR $= 17.5$ dB and SNR $= 26.5$ dB, respectively; and ii) 4×2 and 4×4 OFDM systems at SNR $= 19$ dB and SNR > 30 dB, respectively. *This study shows that the proposed receiver works well even with imperfect receive CSI.*
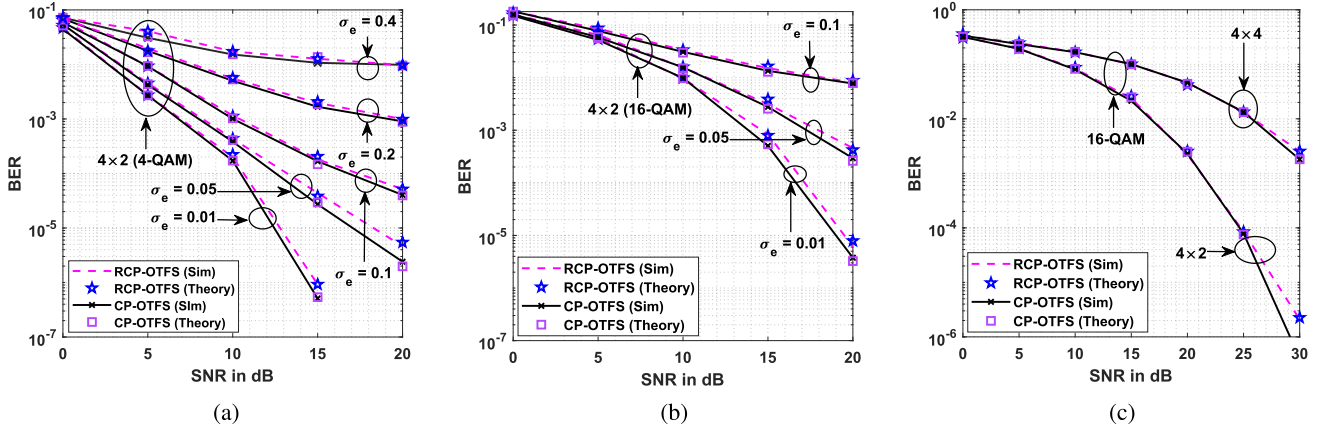
Fig. 8. BER of the proposed receiver using the simulated and analytical BER expressions for (a) 4-QAM, SINR-I; and (b) 16-QAM, SINR-I; and (c) 16-QAM, SINR-D. Here SINR-I denotes that the estimation error σ_e^2 is independent of SNR, and SINR-D denotes that σ_e^2 varies with SNR as $\sigma_e^2 = 1/(N_t * \mathrm{SNR})$. We assume EVA channel with a vehicular speed of 500 kmph. Also $M = 32$ subcarrier and $N = 32$ time slots.
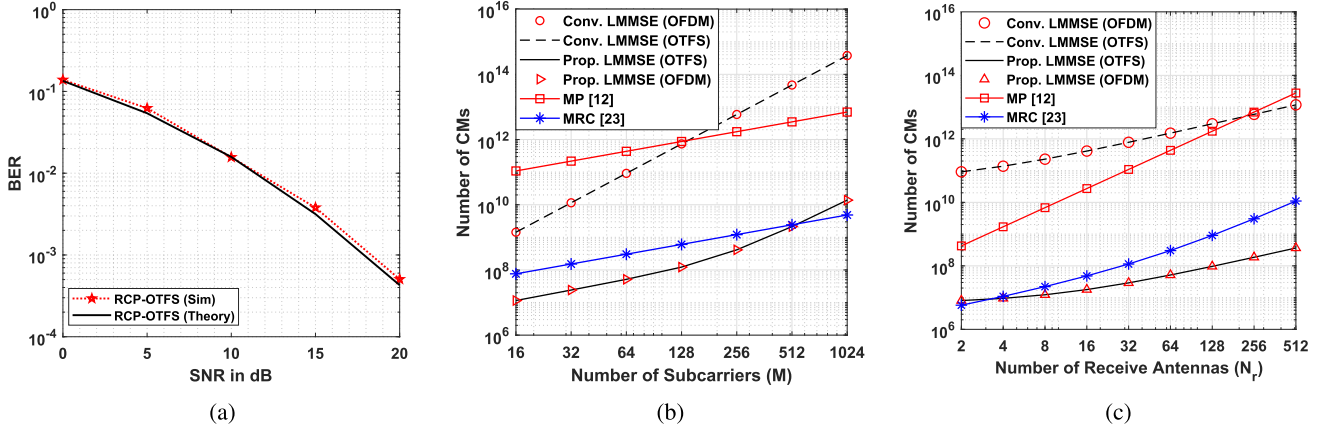

Fig. 9. (a) BER of the proposed receiver using the simulated and analytical BER expressions for 4-QAM with embedded pilot (EP) [54] based channel estimation scheme: $M = N = 32$, $P = 5$, pilot power $E_p = \beta \times$ signal power (E_s) with $\beta = 20$ dB, and EVA channel with a vehicular speed of 500 kmph. Computational complexity comparison of the proposed LMMSE, conventional LMMSE, MP [12] and the MRC [23] receivers with constellation order $Q = 16$, EVA channel [53], number of iterations $N_I = 20$, and (b) $N = 32, M \in [2 \quad 1024]$, $N_r = 64, N_t = 2$; and (c) $M = 64, N = 32$, $N_t = 2, N_r \in [2 \quad 512]$.

C. Comparison of Theoretical and Simulated BER for Proposed LMMSE Receiver With Imperfect Receive CSI

We now validate the BER expression derived in Sec. VI for imperfect receive CSI when channel estimation error variance σ_e^2 is i) independent of SNR; and ii) varies with SNR as $\sigma_e^2 = 1/(N_t * \mathrm{SNR})$ [55]. We compare in Fig. 8a and Fig. 8b the simulated and analytical BER values for the fist case with 4- and 16-QAM constellations, respectively.

We see that the analytical BER, calculated using the SINR derived in (27), closely matches the simulated ones for both RCP- and CP-OTFS systems. *The proposed SINR derivation, and hence the BER derivation is valid even for high σ_e^2 value.* Both simulated and analytical BER values floor at high SNR. This is because in this SNR regime, channel estimation error dominates the error due to noise. We next compare in Fig. 8c the analytical and simulated BERs of the proposed LMMSE receiver for 16-QAM constellations for 4×2 and 4×4 MIMO systems. For this study, we vary error variance as $\sigma_e^2 = 1/(N_t * \mathrm{SNR})$ with $0 \leq \mathrm{SNR} \leq 30$ dB. For $N_t = 4$, σ_e^2 correspondingly varies from 0.25 to 0.25×10^{-3}. We again observe that the analytical and simulated counterparts match.

For example, the analytical and theoretical BER of 10^{-2} is attained at SNR = 17.5 dB and SNR = 25 dB respectively, for both 4×2 and 4×4 RCP MIMO-OTFS systems. This happens due to two main reasons. Firstly, we know that the analytical Q-function expression is a function of the receiver SINR. The proposed analysis accurately models that for the LMMSE receiver considered herein. Secondly, the proposed Algorithm 1, which performs low-complexity inversion of the matrix $\boldsymbol{\Psi}$, does not make any approximations.

We next compare in Fig. 9a the simulated and analytical BER of the proposed receiver by practically estimating the channel using the embedded pilot (EP) based channel estimator from [54]. By employing the full guard along the Doppler axis,[3] and the pilot placement for MIMO-OTFS as per [54, Sec. V-A], the estimate of channel gain for the delay-Doppler propagation path at (k, l)th location between

---

[3]With reduced guard symbols the EP channel estimation model, as shown in [54, Eq. (11)], consists of an additional term $\mathcal{I}[k, l]$, which contains the interference from all the neighboring data symbols [54, Eq. (12)]. The current work, while deriving BER for the proposed LMMSE receiver, does not consider the effect of this interference in the channel estimation error. It is an important direction of study, and can be taken up as future work.

the uth transmit and vth receive antenna can be obtained as $\hat{h}_{u,v}[k,l] = h_{u,v}[k,l] + w_v[k,l]/x_p^u$. Here $w_v[k,l]$ is the zero mean complex Gaussian noise at the vth receive antenna with variance σ^2 and x_p^u is the pliot symbol send by the uth antenna. The channel estimation error $\Delta h_{u,v} = \hat{h}_{u,v}[k,l] - h_{u,v}[k,l]$ is distributed as $\mathcal{CN}(0, 1/(\beta * \text{SNR}))$, where $\text{SNR} = 1/\sigma^2$ (assuming unity signal power) and β is a factor for boosting pilot power [23]. We see that the channel estimation error variance $\sigma_e^2 = 1/(N_t * \text{SNR})$ used in Fig. 8c follows the same formulation where N_t can be considered as the pilot power boosting factor. This is equivalent to our ealier method for modelling the channel estimation error in (25). This is also validated in Fig. 9a, wherein the analytical and simulated BER of the proposed receiver matches for the EP-based practical channel estimator.

D. Computational Complexity Comparison of the Proposed and Conventional LMMSE Receivers

We now compare the analytical computational complexities of the proposed LMMSE receiver, summarized in Table II, and the MP, MRC and the conventional LMMSE MIMO-OTFS receivers. This study only plots the numerical value of the complexity expressions by substituting the relevant parameter values. The computational complexity of the MP detector is $\mathcal{O}(N_t N_r^2 N_I MNP^2 Q)$ [23], where N_I denotes the number iterations required by the MP algorithms to converge, and Q represents the constellation order. The MRC receiver complexity is $N_t NM[(4N_r + N_r^2)L + N_I(3N_r L + 2\log_2 N + 1)] + \mathcal{O}(N_r^3)$ [23], where L is the number of distinct delay taps. We perform the complexity comparison in i) Fig. 9b for $M \in [16\ 1024]$; and ii) Fig. 9c for $N_r \in [2\ 512]$. We compute the worst-case computational complexity of the proposed receiver by considering the upper limit on B_w, which is $2N_t(2\alpha - 1)$ [43], for both RCP- and CP-OTFS systems. The LMMSE receiver complexity of both CP-OTFS and RCP-OTFS systems, as explained in Sec. V, is same. For both MRC and MP receivers, the number of iterations $N_I = 20$ [12], [23]. For the MRC receiver, the parameter $L = P$. We observe from Fig. 9b that for all subcarrier values M, the proposed LMMSE receiver has a significantly lower complexity than the conventional LMMSE and MP receivers. Further, the MRC scheme has a higher complexity than the proposed one for $M < 512$. Its complexity, however, for higher M value, is lower than the proposed receiver. This is due to the increased bandwidth B_w, which increases the proposed receiver complexity.

We next observe from Fig. 9c that the proposed LMMSE receiver has the lowest complexity for different number of receive antennas N_r. For example, for $N_r = 64$, it requires $\mathcal{O}(10^7)$ complex multiplications. This is significantly lower than the MP, MRC and conventional LMMSE receivers, which require $\mathcal{O}(10^{11})$, $\mathcal{O}(10^8)$ and $\mathcal{O}(10^{12})$ complex multiplications, respectively. The complexity gap between the proposed and the MRC receiver increases with N_r. This is because the MRC receiver complexity is proportional to $\mathcal{O}(N_r^3)$, whereas the proposed receiver complexity, as shown in Table-II, varies

linearly with N_r. The MP receiver complexity, due to the N_r^2 term, is higher than even the conventional LMMSE receiver, for high N_r values. These results also show that the proposed low-complexity receiver i) is applicable for highly time varying OFDM systems; and ii) has the same complexity for OTFS and OFDM systems.

VIII. CONCLUSION

We proposed a low-complexity LMMSE receiver for practical-pulse-shaped MIMO reduced CP (RCP)- and CP-OTFS systems. We achieved this objective by exploiting the sparsity and the channel agnostic structure of matrices involved in the equalization. This required establishing that the most computationally-complex operation in a LMMSE OTFS receiver is the inversion of a full-bandwidth positive definite sparse matrix. We reordered this matrix into a sparse-banded matrix, which helped in designing the proposed low-complexity LMMSE receiver, and that too without degrading the BER. We also tightly approximated its SINR, which is used to derived an analytical BER expression for both RCP- and CP-OTFS systems. We showed that the BER provided by this expression, when averaged over multiple channel realizations, accurately matches the one obtained by numerically simulating an OTFS system.

APPENDIX A

We can write $\hat{\Phi}$ using (26) as $\hat{\Phi} = \mathbf{B}^\dagger \left[\widehat{\mathbf{H}}^\dagger \widehat{\mathbf{H}} + \frac{\sigma_n^2}{\sigma_d^2}\mathbf{I}\right]^{-1} \widehat{\mathbf{H}}^\dagger$. This can be further expanded using $\widehat{\mathbf{H}} = \mathbf{H} + \Delta\mathbf{H}$ as

$$\hat{\Phi} = \mathbf{B}^\dagger \left[\mathbf{H}^\dagger \mathbf{H} + \frac{\sigma_n^2}{\sigma_d^2}\mathbf{I} + \mathbf{H}^\dagger \Delta\mathbf{H} + \Delta\mathbf{H}^\dagger \mathbf{H} + \Delta\mathbf{H}^\dagger \Delta\mathbf{H}\right]^{-1}$$
$$\times (\mathbf{H} + \Delta\mathbf{H})^\dagger. \qquad (34)$$

We showed in Fig. 5 that the probability of $||\Delta\mathbf{H}^\dagger \Delta\mathbf{H}||_F \ll ||\Delta\mathbf{H}^\dagger \mathbf{H}||_F$ is very high. We thus neglect $\Delta\mathbf{H}^\dagger \Delta\mathbf{H}$ term in (34), and simplify the expression of $\hat{\Phi}$ as follows

$$\hat{\Phi} \approx \mathbf{B}^\dagger \left[\Psi + \mathbf{T}\right]^{-1}(\mathbf{H}^\dagger + \Delta\mathbf{H}^\dagger)$$
$$= \mathbf{B}^\dagger \left[\mathbf{I} + \Psi^{-1}\mathbf{T}\right]^{-1}\Psi^{-1}(\mathbf{H}^\dagger + \Delta\mathbf{H}^\dagger). \qquad (35)$$

The matrix $\mathbf{T} = \mathbf{H}^\dagger \Delta\mathbf{H} + \Delta\mathbf{H}^\dagger \mathbf{H}$. Recall that $\Psi = \mathbf{H}^\dagger \mathbf{H} + \frac{\sigma_n^2}{\sigma_d^2}\mathbf{I}$. We showed in Sec. VI (Fig. 5a) that the probability $||\Psi^{-1}\mathbf{T}||_F \ll 1$ is close to one. The expression $(\Psi + \mathbf{T})^{-1}$ can therefore be approximated using the first-order Taylor series. We can thus simplify (35) as

$$\hat{\Phi} \approx \mathbf{B}^\dagger \left[\mathbf{I} - \Psi^{-1}\mathbf{T}\right]\Psi^{-1}(\mathbf{H}^\dagger + \Delta\mathbf{H}^\dagger). \qquad (36)$$

In the above equation, we can ignore the terms containing $\mathbf{T}\Delta\mathbf{H}^\dagger$ because $||\Delta\mathbf{H}^\dagger \Delta\mathbf{H}||_F \ll ||\Delta\mathbf{H}^\dagger \mathbf{H}||_F$. We can thus simplify (36) as

$$\hat{\Phi} \approx \underbrace{\mathbf{B}^\dagger \Psi^{-1} \mathbf{H}^\dagger}_{\Phi} \underbrace{-\mathbf{B}^\dagger \Psi^{-1}\mathbf{T}\Psi^{-1}\mathbf{H}^\dagger + \mathbf{B}^\dagger \Psi^{-1}\Delta\mathbf{H}^\dagger}_{\Delta\Phi}. \qquad (37)$$

$$\mathbb{E}\big[\Delta\boldsymbol{\Phi}\mathbf{H}\mathbf{H}^\dagger\Delta\boldsymbol{\Phi}^\dagger\big] \approx \mathbf{B}^\dagger\boldsymbol{\Psi}^{-1}\mathbf{H}^\dagger\mathbb{E}[\Delta\mathbf{H}\boldsymbol{\Omega}^1\Delta\mathbf{H}^\dagger]\mathbf{H}\boldsymbol{\Psi}^{-\dagger}\mathbf{B} + \mathbf{B}^\dagger\boldsymbol{\Psi}^{-1}\mathbb{E}[\Delta\mathbf{H}^\dagger\boldsymbol{\Omega}^2\Delta\mathbf{H}]\boldsymbol{\Psi}^{-\dagger}\mathbf{B}$$
$$- \mathbf{B}^\dagger\boldsymbol{\Psi}^{-1}\mathbb{E}[\Delta\mathbf{H}^\dagger\boldsymbol{\Omega}^3\Delta\mathbf{H}]\boldsymbol{\Psi}^{-\dagger}\mathbf{B} - \mathbf{B}^\dagger\boldsymbol{\Psi}^{-1}\mathbb{E}[\Delta\mathbf{H}^\dagger\boldsymbol{\Omega}^4\Delta\mathbf{H}]\boldsymbol{\Psi}^{-\dagger}\mathbf{B} + \mathbf{B}^\dagger\boldsymbol{\Psi}^{-1}\mathbb{E}[\Delta\mathbf{H}^\dagger\mathbf{H}\mathbf{H}^\dagger\Delta\mathbf{H}]\boldsymbol{\Psi}^{-\dagger}\mathbf{B}.$$
$$(38)$$

$$\mathbb{E}\big[\Delta\boldsymbol{\Phi}\Delta\boldsymbol{\Phi}^\dagger\big] \approx \mathbf{B}^\dagger\boldsymbol{\Psi}^{-1}\mathbf{H}^\dagger\mathbb{E}[\Delta\mathbf{H}\boldsymbol{\Omega}^5\Delta\mathbf{H}^\dagger]\mathbf{H}\boldsymbol{\Psi}^{-\dagger}\mathbf{B} + \mathbf{B}^\dagger\boldsymbol{\Psi}^{-1}\mathbb{E}[\Delta\mathbf{H}^\dagger\boldsymbol{\Omega}^6\Delta\mathbf{H}]\boldsymbol{\Psi}^{-\dagger}\mathbf{B}$$
$$- \mathbf{B}^\dagger\boldsymbol{\Psi}^{-1}\mathbb{E}[\Delta\mathbf{H}^\dagger\boldsymbol{\Omega}^7\Delta\mathbf{H}]\boldsymbol{\Psi}^{-\dagger}\mathbf{B} - \mathbf{B}^\dagger\boldsymbol{\Psi}^{-1}\mathbb{E}[\Delta\mathbf{H}^\dagger\boldsymbol{\Omega}^8\Delta\mathbf{H}]\boldsymbol{\Psi}^{-\dagger}\mathbf{B} + \mathbf{B}^\dagger\boldsymbol{\Psi}^{-1}\mathbb{E}[\Delta\mathbf{H}^\dagger\Delta\mathbf{H}]\boldsymbol{\Psi}^{-\dagger}\mathbf{B}. \quad (39)$$

APPENDIX B

The first and third terms of $\mathbf{R}_\nu$ in (28) are derived by substituting $\Delta\boldsymbol{\Phi}$ from (29) as in (38) and (39), respectively, as shown at the top of this page, where the matrices $\boldsymbol{\Omega}^1, \boldsymbol{\Omega}^5 \in \mathbb{C}^{N_t MN \times N_t MN}$ and $\boldsymbol{\Omega}^2, \boldsymbol{\Omega}^3, \boldsymbol{\Omega}^4, \boldsymbol{\Omega}^6, \boldsymbol{\Omega}^7, \boldsymbol{\Omega}^8 \in \mathbb{C}^{N_r MN \times N_r MN}$ are defined as $\boldsymbol{\Omega}^1 = \boldsymbol{\Psi}^{-1}\mathbf{H}^\dagger\mathbf{H}\mathbf{H}^\dagger\mathbf{H}\boldsymbol{\Psi}^{-\dagger}$, $\boldsymbol{\Omega}^2 = \mathbf{H}\boldsymbol{\Omega}^1\mathbf{H}^\dagger$, $\boldsymbol{\Omega}^3 = \mathbf{H}\mathbf{H}^\dagger\mathbf{H}\boldsymbol{\Psi}^{-\dagger}\mathbf{H}^\dagger$ and $\boldsymbol{\Omega}^4 = \mathbf{H}\boldsymbol{\Psi}^{-1}\mathbf{H}^\dagger\mathbf{H}\mathbf{H}^\dagger$, $\boldsymbol{\Omega}^5 = \boldsymbol{\Psi}^{-1}\mathbf{H}^\dagger\mathbf{H}\boldsymbol{\Psi}^{-\dagger}$, $\boldsymbol{\Omega}^6 = \mathbf{H}\boldsymbol{\Omega}^5\mathbf{H}^\dagger$, $\boldsymbol{\Omega}^7 = \mathbf{H}\boldsymbol{\Psi}^{-1}\mathbf{H}^\dagger$ and $\boldsymbol{\Omega}^8 = \mathbf{H}\boldsymbol{\Psi}^{-\dagger}\mathbf{H}^\dagger$. For evaluating the expectation operations in (38) and (39), we state the following lemmas.

Lemma 2: If each element of the random matrix $\boldsymbol{\mathcal{W}} \in \mathbb{C}^{m\times n}$ is i.i.d. with zero mean and variance σ^2, then for Hermitian matrix $\boldsymbol{\mathcal{R}} \in \mathbb{C}^{n\times n}$ and $\boldsymbol{\mathcal{R}}_1 \in \mathbb{C}^{m\times m}$

$$\mathbb{E}[\boldsymbol{\mathcal{W}}\boldsymbol{\mathcal{R}}_1\boldsymbol{\mathcal{W}}^\dagger] = \frac{\sigma^2}{m}\text{trace}\{\boldsymbol{\mathcal{R}}_1\} \text{ and}$$
$$\mathbb{E}[\boldsymbol{\mathcal{W}}^\dagger\boldsymbol{\mathcal{R}}\boldsymbol{\mathcal{W}}] = \frac{\sigma^2}{n}\text{trace}\{\boldsymbol{\mathcal{R}}\}. \quad (40)$$

Proof: The first result is because of $\mathbb{E}[\mathbf{w}_i^T\boldsymbol{\mathcal{R}}_1\mathbf{w}_j^*] = \sigma^2\text{trace}\{\boldsymbol{\mathcal{R}}_1\}$ for $i = j$ and 0 otherwise. Here $\mathbf{w}_i^T$ is the ith row of the matrix $\boldsymbol{\mathcal{W}}$. The second result can be similarly derived. ∎

Lemma 3: For a random matrix $\boldsymbol{\mathcal{W}} \in \mathbb{C}^{m\times n}$ with i.i.d. zero-mean elements and variance σ^2, and deterministic matrices $\boldsymbol{\mathcal{A}} \in \mathbb{C}^{n\times n}$, $\boldsymbol{\mathcal{B}} \in \mathbb{C}^{m\times m}$, then $\mathbb{E}[\boldsymbol{\mathcal{W}}\boldsymbol{\mathcal{A}}\boldsymbol{\mathcal{W}}] = \mathbf{0}$ and $\mathbb{E}[\boldsymbol{\mathcal{W}}^\dagger\boldsymbol{\mathcal{B}}\boldsymbol{\mathcal{W}}^\dagger] = \mathbf{0}$.

Proof: The first result follows from the property $\mathbb{E}[\mathbf{w}_i\boldsymbol{\mathcal{A}}\mathbf{w}_j] = \mathbf{0}$, and the second one is due to the fact that $\mathbb{E}[\mathbf{w}_i^\dagger\boldsymbol{\mathcal{B}}\mathbf{w}_j^\dagger] = \mathbf{0}$. ∎

Lemma 4: For MIMO-OTFS estimation error channel matrix $\Delta\mathbf{H}$,

$$\mathbb{E}\big[\Delta\mathbf{H}\Delta\mathbf{H}^\dagger\big] = \sigma_e^2 P N_t\mathbf{I} \text{ and } \mathbb{E}\big[\Delta\mathbf{H}^\dagger\Delta\mathbf{H}\big] = \sigma_e^2 P N_r\mathbf{I}. \quad (41)$$

Proof: We prove this lemma for the RCP-OTFS system. It can similarly be proved for a CP-OTFS system. Since the structure of $\Delta\mathbf{H}$ is same as that of $\mathbf{H}$, we can split it using (8) as

$$\Delta\mathbf{H} = \begin{bmatrix} \Delta\mathbf{H}_{1,1} & \cdots & \Delta\mathbf{H}_{N_t,1} \\ \vdots & \ddots & \vdots \\ \Delta\mathbf{H}_{1,N_r} & \cdots & \Delta\mathbf{H}_{N_t,N_r} \end{bmatrix}. \quad (42)$$

We assume that the channel estimation error values from different transmit-receive antenna pairs are uncorrelated [56]. This implies that $\mathbb{E}\big[\Delta\mathbf{H}_{u_1,v_1}\Delta\mathbf{H}_{u,v}^\dagger\big] = 0$ for $u \neq u_1$ and

$v \neq v_1$. We can thus compute $\mathbb{E}\big[\Delta\mathbf{H}\Delta\mathbf{H}^\dagger\big]$ by using (42) and above-mentioned property as

$$\mathbb{E}\big[\Delta\mathbf{H}\Delta\mathbf{H}^\dagger\big] = \sum_{i=1}^{N_t}\mathbb{E}\big[\Delta\mathbf{H}_{i,i}\Delta\mathbf{H}_{i,i}^\dagger\big]\mathbf{I}. \quad (43)$$

The error in $\mathbf{H}$ occurs due to the estimation of channel coefficients $h_p^{(u,v)}$ in (9). We can thus write estimated channel coefficient as $\hat{h}_p^{(u,v)} = h_p^{(u,v)} + \delta h_p^{(u,v)}$, where the error component $\delta h_p^{(u,v)} \sim \mathcal{CN}(0, \sigma_e^2)$. Using (9), estimated MIMO channel matrix can be written as

$$\widehat{\mathbf{H}}_{u,v} = \underbrace{\sum_{p=1}^P h_p^{(u,v)}\boldsymbol{\Pi}^{l_p^{(u,v)}}\boldsymbol{\Delta}^{k_p^{(u,v)}}}_{\mathbf{H}_{u,v}} + \underbrace{\sum_{p=1}^P \delta h_p^{(u,v)}\boldsymbol{\Pi}^{l_p^{(u,v)}}\boldsymbol{\Delta}^{k_p^{(u,v)}}}_{\Delta\mathbf{H}_{u,v}}. \quad (44)$$

The expression $\mathbb{E}\big[\Delta\mathbf{H}_{u,v}\Delta\mathbf{H}_{u,v}^\dagger\big]$ is then simplified using (44) as

$$\mathbb{E}\big[\Delta\mathbf{H}_{u,v}\Delta\mathbf{H}_{u,v}^\dagger\big]$$
$$= \mathbb{E}\Bigg[\sum_{p=1}^P \delta h_p^{(u,v)}\boldsymbol{\Pi}^{l_p^{(u,v)}}\boldsymbol{\Delta}^{k_p^{(u,v)}}$$
$$\times \sum_{q=1}^P \delta h_q^{(u,v)*}\boldsymbol{\Delta}^{-k_q^{(u,v)}}\boldsymbol{\Pi}^{-l_q^{(u,v)}}\Bigg] = \sum_{p=q=1}^P \mathbb{E}\big[|\delta h_p^{(u,v)}|^2\big]$$
$$+ \sum_p\sum_{\substack{q \\ p\neq q}}\underbrace{\mathbb{E}\big[\delta h_p^{(u,v)}\delta h_q^{(u,v)*}\big]}_{=\,0}\boldsymbol{\Pi}^{l_p^{(u,v)}}\boldsymbol{\Delta}^{k_p^{(u,v)}}\boldsymbol{\Delta}^{-k_q^{(u,v)}}\boldsymbol{\Pi}^{-l_q^{(u,v)}}$$
$$= P\sigma_e^2. \quad (45)$$

We can now simplify (43) using (45) as $\mathbb{E}\big[\Delta\mathbf{H}\Delta\mathbf{H}^\dagger\big] = \sigma_e^2 P N_t\mathbf{I}$, and similarly show that $\mathbb{E}\big[\Delta\mathbf{H}^\dagger\Delta\mathbf{H}\big] = \sigma_e^2 P N_r\mathbf{I}$. ∎

Simplification of (38) and (39) using *Lemma* 2, *Lemma* 3 and *Lemma* 4 yields the desired results for the expression $\mathbb{E}\big[\Delta\boldsymbol{\Phi}\mathbf{H}\mathbf{H}^\dagger\Delta\boldsymbol{\Phi}^\dagger\big]$ and $\mathbb{E}\big[\Delta\boldsymbol{\Phi}\Delta\boldsymbol{\Phi}^\dagger\big]$ in (30) and (31), respectively.

REFERENCES

[1] S. K. Mohammed, "Derivation of OTFS modulation from first principles," *IEEE Trans. Veh. Technol.*, vol. 70, no. 8, pp. 7619–7636, Aug. 2021.

[2] V. Khammammetti and S. K. Mohammed, "OTFS-based multiple-access in high Doppler and delay spread wireless channels," *IEEE Wireless Commun. Lett.*, vol. 8, no. 2, pp. 528–531, Apr. 2019.

[3] K. Deka, A. Thomas, and S. Sharma, "OTFS-SCMA: A code-domain NOMA approach for orthogonal time frequency space modulation," *IEEE Trans. Commun.*, vol. 69, no. 8, pp. 5043–5058, Aug. 2021.

[4] S. Li, J. Yuan, W. Yuan, Z. Wei, B. Bai, and D. W. K. Ng, "Performance analysis of coded OTFS systems over high-mobility channels," *IEEE Trans. Wireless Commun.*, vol. 20, no. 9, pp. 6033–6048, Sep. 2021.

[5] H. Qu, G. Liu, L. Zhang, M. A. Imran, and S. Wen, "Low-dimensional subspace estimation of continuous-Doppler-spread channel in OTFS systems," *IEEE Trans. Commun.*, vol. 69, no. 7, pp. 4717–4731, Jul. 2021.

[6] Y. Ge, Q. Deng, P. C. Ching, and Z. Ding, "Receiver design for OTFS with a fractionally spaced sampling approach," *IEEE Trans. Wireless Commun.*, vol. 20, no. 7, pp. 4072–4086, Jul. 2021.

[7] L. Gaudio, M. Kobayashi, G. Caire, and G. Colavolpe, "On the effectiveness of OTFS for joint radar parameter estimation and communication," *IEEE Trans. Wireless Commun.*, vol. 19, no. 9, pp. 5951–5965, Sep. 2020.

[8] S. Tiwari, S. S. Das, and V. Rangamgari, "Low complexity LMMSE receiver for OTFS," *IEEE Commun. Lett.*, vol. 23, no. 12, pp. 2205–2209, Dec. 2019.

[9] G. D. Surabhi and A. Chockalingam, "Low-complexity linear equalization for OTFS modulation," *IEEE Commun. Lett.*, vol. 24, no. 2, pp. 330–334, Feb. 2020.

[10] G. D. Surabhi, R. M. Augustine, and A. Chockalingam, "On the diversity of uncoded OTFS modulation in doubly-dispersive channels," *IEEE Trans. Wireless Commun.*, vol. 18, no. 6, pp. 3049–3063, Jun. 2019.

[11] R. Hadani et al., "Orthogonal time frequency space modulation," in *Proc. IEEE Wireless Commun. Netw. Conf. (WCNC)*, San Francisco, CA, USA, Mar. 2017, pp. 1–6.

[12] P. Raviteja, K. T. Phan, Y. Hong, and E. Viterbo, "Interference cancellation and iterative detection for orthogonal time frequency space modulation," *IEEE Trans. Wireless Commun.*, vol. 17, no. 10, pp. 6501–6515, Oct. 2018.

[13] H. Zhang and T. Zhang, "A low-complexity message passing detector for OTFS modulation with probability clipping," *IEEE Wireless Commun. Lett.*, vol. 10, no. 6, pp. 1271–1275, Jun. 2021.

[14] W. Yuan, Z. Wei, J. Yuan, and D. W. K. Ng, "A simple variational Bayes detector for orthogonal time frequency space (OTFS) modulation," *IEEE Trans. Veh. Technol.*, vol. 69, no. 7, pp. 7976–7980, Apr. 2020.

[15] K. R. Murali and A. Chockalingam, "On OTFS modulation for high-Doppler fading channels," in *Proc. Inf. Theory Appl. Workshop (ITA)*, San Diego, CA, USA, Feb. 2018, pp. 1–10.

[16] J. Cheng, H. Gao, W. Xu, Z. Bie, and Y. Lu, "Low-complexity linear equalizers for OTFS exploiting two-dimensional fast Fourier transform," 2019, *arXiv:1909.00524*.

[17] M. K. Ramachandran, G. D. Surabhi, and A. Chockalingam, "OTFS: A new modulation scheme for high-mobility use cases," *J. Indian Inst. Sci.*, vol. 100, no. 2, pp. 315–336, Apr. 2020, doi: 10.1007/s41745-020-00167-4.

[18] G. D. Surabhi and A. Chockalingam, "Low-complexity linear equalization for 2×2 MIMO-OTFS signals," in *Proc. IEEE 21st Int. Workshop Signal Process. Adv. Wireless Commun. (SPAWC)*, Atlanta, GA, USA, May 2020, pp. 1–5.

[19] P. Singh, A. Gupta, H. B. Mishra, and R. Budhiraja, "Low-complexity ZF/MMSE MIMO-OTFS receivers for high-speed vehicular communication," *IEEE Open J. Commun. Soc.*, vol. 3, pp. 209–227, 2022.

[20] H. Qu, G. Liu, L. Zhang, S. Wen, and M. A. Imran, "Low-complexity symbol detection and interference cancellation for OTFS system," *IEEE Trans. Commun.*, vol. 69, no. 3, pp. 1524–1537, Mar. 2021.

[21] B. C. Pandey, S. K. Mohammed, P. Raviteja, Y. Hong, and E. Viterbo, "Low complexity precoding and detection in multi-user massive MIMO OTFS downlink," *IEEE Trans. Veh. Technol.*, vol. 70, no. 5, pp. 4389–4405, May 2021.

[22] H. B. Mishra, P. Singh, A. K. Prasad, and R. Budhiraja, "OTFS channel estimation and data detection designs with superimposed pilots," *IEEE Trans. Wireless Commun.*, vol. 21, no. 4, pp. 2258–2274, Apr. 2022.

[23] T. Thaj and E. Viterbo, "Low-complexity linear diversity-combining detector for MIMO-OTFS," *IEEE Wireless Commun. Lett.*, vol. 11, no. 2, pp. 288–292, Feb. 2022.

[24] T. Thaj and E. Viterbo, "Low complexity iterative rake decision feedback equalizer for zero-padded OTFS systems," *IEEE Trans. Veh. Technol.*, vol. 69, no. 12, pp. 15606–15622, Dec. 2020.

[25] M. K. Ramachandran and A. Chockalingam, "MIMO-OTFS in high-Doppler fading channels: Signal detection and channel estimation," in *Proc. IEEE Global Commun. Conf. (GLOBECOM)*, Abu Dhabi, UAE, Dec. 2018, pp. 206–212.

[26] S. Li et al., "Hybrid MAP and PIC detection for OTFS modulation," *IEEE Trans. Veh. Technol.*, vol. 70, no. 7, pp. 7193–7198, Jul. 2021.

[27] S. Li, W. Yuan, Z. Wei, and J. Yuan, "Cross domain iterative detection for orthogonal time frequency space modulation," *IEEE Trans. Wireless Commun.*, vol. 21, no. 4, pp. 2227–2242, Apr. 2022.

[28] P. Singh, H. B. Mishra, and R. Budhiraja, "Low-complexity linear MIMO-OTFS receivers," in *Proc. IEEE Int. Conf. Commun. Workshops (ICC Workshops)*, Montreal, QC, Canada, Jun. 2021, pp. 1–6.

[29] B. Boashash, *Time-Frequency Signal Analysis and Processing: A Comprehensive Reference*. New York, NY, USA: Academic, 2015.

[30] W. Kozek and A. F. Molisch, "Nonorthogonal pulseshapes for multicarrier communications in doubly dispersive channels," *IEEE J. Sel. Areas Commun.*, vol. 16, no. 8, pp. 1579–1589, Oct. 1998.

[31] P. Raviteja, Y. Hong, E. Viterbo, and E. Biglieri, "Practical pulse-shaping waveforms for reduced-cyclic-prefix OTFS," *IEEE Trans. Veh. Tech.*, vol. 68, no. 1, pp. 957–961, Jan. 2019.

[32] S. Tiwari and S. S. Das, "Circularly pulse-shaped orthogonal time frequency space modulation," *Electron. Lett.*, vol. 56, no. 3, pp. 157–160, Feb. 2020.

[33] M. Rupp, S. Schwarz, and M. Taranetz, *The Vienna LTE-Advanced Simulators*. Singapore: Springer, 2016.

[34] K. E. Atkinson, *An Introduction to Numerical Analysis*, vol. 19781. New York, NY, USA: Wiley, 1989.

[35] P. A. Bello, "Characterization of randomly time-variant linear channels," *IEEE Trans. Commun. Syst.*, vol. CS-11, no. 4, pp. 360–393, Dec. 1963.

[36] G. H. Golub and C. F. Van Loan, *Matrix Computations*, vol. 3. Baltimore, MD, USA: JHU Press, 2012.

[37] P. Wei, X.-G. Xia, Y. Xiao, and S. Li, "Fast DGT-based receivers for GFDM in broadband channels," *IEEE Trans. Commun.*, vol. 64, no. 10, pp. 4331–4345, Oct. 2016.

[38] P. Singh, E. Sharma, K. Vasudevan, and R. Budhiraja, "CFO and channel estimation for frequency selective MIMO-FBMC/OQAM systems," *IEEE Wireless Commun. Lett.*, vol. 7, no. 5, pp. 844–847, Oct. 2018.

[39] J. F. Kepler, T. P. Krauss, and S. Mukthavaram, "Delay spread measurements on a wideband MIMO channel at 3.7 GHz," in *Proc. IEEE 56th Veh. Tech. Conf.*, vol. 4, Sep. 2002, pp. 2498–2502.

[40] T. Rautiainen, G. Wölfle, and R. Hoppe, "Verifying path loss and delay spread predictions of a 3D ray tracing propagation model in urban environment," in *Proc. IEEE 56th Veh. Technol. Conf.*, vol. 4, Dec. 2002, pp. 2470–2474.

[41] J. A. George, "Computer implementation of the finite element method," Stanford Univ., Stanford, CA, USA, Tech. Rep. STAN-CS-7J-208, Feb. 1971. [Online]. Available: https://apps.dtic.mil/sti/citations/AD0726171

[42] E. H. Cuthill and J. McKee, "Reducing the bandwidth of sparse symmetric matrices," in *Proc. ACM 24th Nat. Conf.*, vol. 1969, 1969, pp. 157–172.

[43] N. E. Gibbs, W. G. Poole, Jr., and P. K. Stockmeyer, "An algorithm for reducing the bandwidth and profile of a sparse matrix," *SIAM J. Numer. Anal.*, vol. 13, no. 2, pp. 236–250, Apr. 1976, doi: 10.1137/0713023.

[44] D. W. Walker, T. Aldcroft, A. Cisneros, G. C. Fox, and W. Furmanski, "LU decomposition of banded matrices and the solution of linear systems on hypercubes," in *Proc. 3rd Conf. Hypercube Concurrent Comput. Appl. (CP)*, vol. 2, 1988, pp. 1635–1655.

[45] S. S. Das, V. Rangamgari, S. Tiwari, and S. C. Mondal, "Time domain channel estimation and equalization of CP-OTFS under multiple fractional dopplers and residual synchronization errors," *IEEE Access*, vol. 9, pp. 10561–10576, 2021.

[46] S. S. Das, E. D. Carvalho, and R. Prasad, "Performance analysis of OFDM systems with adaptive sub carrier bandwidth," *IEEE Trans. Wireless Commun.*, vol. 7, no. 4, pp. 1117–1122, Apr. 2008.

[47] F. Hlawatsch and G. Matz, *Wireless Communications Over Rapidly Timevarying Channels*. New York, NY, USA: Academic, 2011.

[48] C. Wang, E. K. S. Au, R. D. Murch, W. H. Mow, R. S. Cheng, and V. Lau, "On the performance of the MIMO zero-forcing receiver in the presence of channel estimation error," *IEEE Trans. Wireless Commun.*, vol. 6, no. 3, pp. 805–810, Mar. 2007.

[49] P. Singh, H. B. Mishra, A. K. Jagannatham, and K. Vasudevan, "Semi-blind, training, and data-aided channel estimation schemes for MIMO-FBMC-OQAM systems," *IEEE Trans. Signal Process.*, vol. 67, no. 18, pp. 4668–4682, Sep. 2019.

[50] A. Edelman and N. Rao, "Random matrix theory," *Acta Numer.*, vol. 14, pp. 233–297, Jan. 2005.

[51] E. Eraslan, B. Daneshrad, and C. Y. Lou, "Performance indicator for MIMO MMSE receivers in the presence of channel estimation error," *IEEE Wireless Commun. Lett.*, vol. 2, no. 2, pp. 211–214, Apr. 2013.

[52] Y.-P. Lin, S.-M. Phoong, and P. Vaidyanathan, *Filter Bank Transceivers for OFDM and DMT Systems*. Cambridge, U.K.: Cambridge Univ. Press, 2010.

[53] M. Series, "Guidelines for evaluation of radio interface technologies for IMT-advanced," ITU, Geneva, Switzerland, Tech. Rep., 2135-1, 2009.

[54] P. Raviteja, K. T. Phan, and Y. Hong, "Embedded pilot-aided channel estimation for OTFS in delay–Doppler channels," *IEEE Trans. Veh. Technol.*, vol. 68, no. 5, pp. 4906–4917, May 2019.

[55] B. Hassibi and B. M. Hochwald, "How much training is needed in multiple-antenna wireless links?" *IEEE Trans. Inf. Theory*, vol. 49, no. 4, pp. 951–963, Apr. 2003.

[56] P. Singh, R. Budhiraja, and K. Vasudevan, "SER analysis of MMSE combining for MIMO FBMC-OQAM systems with imperfect CSI," *IEEE Commun. Lett.*, vol. 23, no. 2, pp. 226–229, Feb. 2019.

Shashank Tiwari received the M.Tech. and Ph.D. degrees from the Indian Institute of Technology Kharagpur, Kharagpur, India, in 2011 and 2021, respectively. He has been working as a Senior Specialist at Nokia Networks, Bengaluru, since August 2021. He worked as a Project Executive Officer at IIT Kanpur from January 2021 to June 2021. He served as a Faculty Member at the LNM Institute of Information Technology, Jaipur, India, from 2011 to 2013. His research interests include wireless communications, digital signal processing for communications, and 5G waveform design.

Prem Singh received the M.Tech. and Ph.D. degrees in electrical engineering from the Indian Institute of Technology Kanpur, India, in 2011 and 2020, respectively. He worked as a Project Executive Officer on the Indigenous 5G TestBed project, where he designed FPGA based hardware and software algorithms for an end-to-end 3GPP compliant 5G-NR Testbed. He is currently working as an Assistant Professor at IIIT Bangalore, India. His Ph.D. thesis received the Best Thesis Award in IEEE CICT 2020 organized by IIIT Kancheepuram, India, and was one of the finalists (top two) for the Indian National Academy of Engineering (INAE) Innovative Student Project Award 2021. His two recent research papers were picked by the IEEE Communication Society for the best readings for OTFS and Delay-Doppler signal processing. His student's paper was one of the finalists for the best student paper award at the IEEE SPCOM, IISc Bengaluru, in July 2022. His current research interests lie in the area of parameter estimation and transceiver design for 5G and beyond wireless technologies, including orthogonal time-frequency space (OTFS), filter bank multicarrier (FBMC), massive MIMO, and millimeter-wave. His interests also include designing practical 4G/5G wireless systems using 3GPP standards.

Rohit Budhiraja (Member, IEEE) received the M.S. degree in electrical engineering and the Ph.D. degree from IIT Madras in 2004 and 2015, respectively. From 2004 to 2011, he worked for two start-ups, where he designed both hardware and software algorithms, from scratch, for physical layer processing of WiMAX- and LTE-based cellular systems. He is currently an Assistant Professor with IIT Kanpur, where he is also leading an effort to design a 5G research testbed. His current research interests include design of energy-efficient transceiver algorithms for 5G massive MIMO and full-duplex systems, robust precoder design for wireless relaying, machine learning methods for channel estimation in mm-wave systems, and spatial modulation system design. His paper was shortlisted as one of the finalists for the Best Student Paper Awards at the IEEE International Conference on Signal Processing and Communications, Benagluru, India, in 2014. He also received IIT Madras Research Award for the quality and quantity of research work done in the Ph.D. degree, Early Career Research Award, and Teaching Excellence Certificate at IIT Kanpur.